DYNAMICS OF FINITE-DENSITY INERTIAL PARTICLES IN AN ARBITRARY FLOW

A Thesis

Presented to the Faculty of the Graduate School

of Cornell University

in Partial Fulfillment of the Requirements for the Degree of

Master of Science

by

Anirban Bhattacharjee

August 2021

ABSTRACT

Anirban Bhattacharjee

The main focus of this thesis is the dynamics of finite-density inertial particles in an arbitrary flow. We derive a closed-form solution for the Lyapunov exponent, which measures the rate of change of volume of a cloud of particles. At an infinite density ratio, it has been shown [1] that much of the clustering phenomenon in 3D turbulence can be explained using a 1D canonical flow oscillating at a single frequency. We extend this analysis to study the dynamics of various particles, namely light, heavy and neutrally buoyant for a wide range of flows. We know that clustering is negligible at small and large Stokes number and substantial at Stokes number $\approx O(1)$. We analytically explain this non-monotonic behavior for finite-density particles heavier than the fluid and study the effect of density ratio for such particles in turbulence. We also observe a lower bound of -1/2 on the Lyapunov exponent normalized by the particle relaxation time, but there is no such upper bound. We further observe that neutrally buoyant particles disperse in a strongly straining flow. Finally, we explain the effect of the Basset term on our analysis.

This thesis also contributes to developing an efficient solver called complex-valued Stokes Solver (SCVS) for cardiovascular flows, which solves the unsteady Stokes equation in the spectral domain instead of solving it in the time domain. SCVS shows an order of magnitude improvement in accuracy and two orders of magnitude improvement in cost compared to a standard stabilized finite element solver called RBVMS. For a more direct one-to-one comparison, we also compare SCVS against an in-house time-based Stokes solver, which uses

the same shape functions, where we see three orders of magnitude improvement in the cost and improved accuracy. This improvement in performance stems from the transformation of the governing differential equations into a system of boundary value problems, where only a few modes need to be solved instead of thousands of time steps.

BIOGRAPHICAL SKETCH

Anirban Bhattacharjee was born in Asansol, a small city in the eastern state of West Bengal, India. An unwavering love for Physics and Mathematics coupled with a penchant for solving complicated problems and puzzles in high school made him choose the path of engineering. He did his undergraduate studies at the Indian Institute of Technology, Kharagpur, where he developed a passion for fluid mechanics and applied mathematics. During his time at Kharagpur, he researched microfluidics, particularly on the topics of droplet microfluidics and electro-osmotic flows. He also did a research internship at University of Laval, Canada where he worked on the effect of air velocity and buoyancy on the Saffman-Taylor instability problem for yield-stress fluids. To further pursue a career in research, Anirban decided to join Cornell University as a graduate student in the Sibley School of Mechanical and Aerospace Engineering. He worked on particle clustering and contributed to a project carried out by Chenwei (Andy) Meng [2] on the topic of Stokes Solver for cardiovascular flows. That is the subject of this thesis.

This document is dedicated to all Cornell graduate students.

ACKNOWLEDGEMENTS

I would like to thank my advisor Prof. Mahdi Esmaily for his continuous input and support during my graduate studies. His advice and suggestions helped me develop my academic and interpersonal skills. I would also like to thank Prof. Perrine Pepiot and Prof. Alex Townsend for their advice and inputs related to my project.

I would like to extend my gratitude to Grant Rydquist and Chenwei Meng for answering all my queries related to Fortran programming and High Performance Computing, no matter how trivial they were. I would also like to thank Soumyamouli Pal, Ritabrata Ray, Varinderjit Mann, Sounak Maji, Ankush Mukherjee, Ali Amadeh, Pusham Sharma and Shayak Bhattacharjee for their friendship and support.

I would finally like to thank my parents and my girlfriend for their continuous support during my ups and downs and for encouraging me to continue following my dreams.

TABLE OF CONTENTS

LIST OF TABLES

LIST OF FIGURES

CHAPTER 1

INTRODUCTION

1.1 Motivation

The dynamics of particles in arbitrary flows has been a keen area of interest for decades since not only is it ubiquitous [3, 4], but also a better understanding of it improves the design of several applications and helps to identify new ones. The study of droplet coalescence in clouds [5, 6, 7] can improve weather forecasting tools. The study of planktons [4] and marine snow in the oceans [8] is very important since they play a major role in sustaining food webs and global biochemical cycles, mainly the carbon cycle. It also has many other applications in science and engineering, ranging from pharmaceutical to energy. [9, 10, 11, 12]

One interesting phenomenon often observed is the formation of regions of high concentration by inertial particles in arbitrary flows. This is known as particle clustering [13], preferential concentration [14] or segregation [15]. We focus on an ensemble of particles which we call a cloud. Our goal is to develop a simple analytical model that predicts what happens to the cloud of particles at different values of particle-to-fluid density ratio and Stokes number. Subjected to a background flow, the cloud can either grow in size, which we call dispersion or shrink over time, which we call clustering. Although there has been extensive numerical and experimental research on these phenomena in the past, there is no analytical model to predict the dynamics of a cloud of finite-density inertial particles. The first part of the thesis addresses that.

In the second part of the thesis, our focus is on developing an efficient Stokes solver for cardiovascular flows. Developing efficient modeling tools is paramount since heart-related conditions are the leading cause of death worldwide [16]. In many cases, the simulation of blood flow needs to be fast and cost-effective since time is an important constraint. One needs to remember that cardiovascular modeling has to be often done in complex geometries. One important application, keeping in mind all these requirements is treating patients with congenital heart defects who need to be operated on immediately after birth [17]. Also, performing shape optimization and uncertainty quantification for surgery related purposes require hundreds of simulations [18]. In industries, where there is a constraint on the access to computational resources due to cost considerations [19], there arises a need to build computationally efficient techniques. We try to develop such a technique and see how it reduces the CPU usage and improves the accuracy.

1.2 Previous Work

The effect of the Stokes number and the flow Reynolds number on particle dynamics has been extensively studied, which include not only experimental research [10, 20, 21, 22, 23, 24] but also numerical [25, 26, 27, 15, 28, 29] and analytical predictions [30, 13, 31, 32, 33]. It has been shown in these papers that there is minimum clustering at small Stokes numbers, where the particles act as fluid tracers and simply move along the streamlines of the flow. In contrast, at very large Stokes number, the particle motion is uncorrelated with the background flow and they disperse out ballistically due to their large inertia. Maximum clustering occurs at Stokes number $\approx O(1)$. Although this non-monotonic

behavior has been observed experimentally and validated numerically, it has not been explained analytically. Recently, this phenomenon has been analytically explained in [1], where the particle-to-fluid density ratio was assumed to be infinitely large. We will call the analysis IDR, where IDR stands for Infinite Density Ratio.

One of the first analytical relations of particle clustering was derived by [32] and [33]. We will call this analysis RM (which stands for Robinson–Maxey) throughout the rest of our work and this is derived by assuming that the acceleration of the particles is roughly the same as that of the fluid. We will show later that the amount of clustering or dispersion which is quantified by a parameter C (which is defined in Section 2.1) equals another parameter, Q, which is half the Q-criterion defined in [34, 35] used for the identification of vortical regions. RM predicts that C changes linearly with Q unbounded which is not consistent with experimental observations. The drawback of this analysis stems from its central assumption that the acceleration of the particles is the same as that of the background flow. This assumption is only valid when the particle inertia is very small and hence it restricts the validity of RM to small Stokes number.

For Stokes number $\approx O(1)$ or higher, IDR however explains the non-monotonic behavior analytically. The central assumption in IDR is that the particle-to-fluid density ratio is infinite and it only takes the drag force into account. It also makes use of a 1D canonical flow with a single frequency of oscillation to explain the aforementioned behavior, which we will talk about in greater detail later. There is no analytical study however on the dynamics of finite-density inertial particles and we plan to extend this canonical flow to

investigate the more realistic scenario of finite particle-to-fluid density ratio.

Next, we shift our focus to some of the previous work on solvers for cardiovascular flows. Although there is a wide variety of available numerical methods for simulating cardiovascular flows, we focus mainly on finite element techniques to demonstrate the relative accuracy and cost of our proposed technique because first, they are widely adopted [36] and second, our technique is also based on finite element modeling. The Residual-based variational multiscale method (RBVMS) is a standard finite element based time-dependent solver, which uses the concept of the streamwise upwind Petrov-Galerkin (SUPG) technique [37, 38, 39]. For time-dependent solvers like the RBVMS, one needs to discretize the differential equations, i.e. divide the entire time domain of the problem into small time steps. These time steps should be small enough to ensure that the solver is not only accurate but is also stable. Hence the cost depends on the size of these time steps. The cost gets increased further when one needs to perform many simulations to get a cycle-to-cycle convergence, given the transient nature of the solution.

To get rid of these issues, one can transform the whole problem from the time domain to the frequency domain using Fourier transformation. This was the main subject of Chenwei Meng's thesis [2]. Instead of now solving for thousands of time steps, one needs to solve multiple boundary problems, each corresponding to one mode. For cardiovascular flows, it was shown that the number of modes required to get an accurate solution is significantly less (less than ten) than the number of time steps required to solve a single cardiac cycle (in the order of thousands [40]). Thus, the accuracy or the stability of the scheme no longer depends on the step size since the technique gets rid of the time-

integration scheme completely. We need not worry about the cycle-to-cycle convergence as well since we are solving boundary value problems and that does not include the transient part of the solution. This technique shows a significant improvement in the accuracy and cost compared to RBVMS.

In this study, we compare the performance of this spectral solver with the Mixed-Shape Stokes (MSS) solver which we will talk about in greater detail later. The MSS is tailored to be closer to the proposed technique for a more apple-to-apple comparison.

1.3 Overview

The objective of chapter 2 is to study the effect of particle-to-fluid density ratio and the Stokes number on clustering. We start with the governing differential equations and derive a relation for the Lyapunov exponent. Then, we use a simple model to verify that our analytical results agree well with the reference numerical results. Next, we show that this analysis is also valid at small Stokes number (RM) and infinite particle-to-fluid density ratios (IDR). We explain the non-monotonic behavior of clustering for particles in turbulence but restrict it to heavy particles. Then we derive the results for extremely light and neutrally buoyant particles. Finally, we look at what happens if we include the Basset history term, a term that we have neglected otherwise.

In chapter 3, we first introduce the spectral algorithm, which we call complex-valued Stokes solver (SCVS). Next, we compare the performance of SCVS against a standard RBVMS solver for oscillating flows in a 3D pipe. We also compare SCVS to an in-house MSS solver before drawing conclusions. Fi-

nally, we present the preliminary results on an inherently parallel GMRES in chapter 4.

CHAPTER 2

DYNAMICS OF FINITE-DENSITY PARTICLES

2.1 Introduction

Particle dynamics is determined by many parameters such as the particle size, the particle-to-fluid density ratio, thermal fluctuations, the anisotropy of the background flow, the Reynolds number, and the Froude number. To ensure that our analysis is tractable, we ignore those parameters that have a negligible effect on the dynamics. The thermal fluctuations are neglected because the Knudsen number is small. Similarly, the body forces are assumed to be too small to have any significant effect since the Froude number is large. We also assume that the flow is isotropic. Further, we neglect the effect of particles on flow and particle-particle interactions because we assume that the volume fraction is low. We are interested in the Batchelor regime, where the particles are smaller than the Kolmogorov length scale, η. With the assumptions above, the dynamics depend on the Stokes number, St and the particle-to-fluid density ratio, ρ_p/ρ_f, where ρ_p and ρ_f are the particle and fluid densities, respectively.

It was shown in IDR that the motion of the particles in the cloud in three dimensions can be analyzed as three one-dimensional problems. The velocity gradient tensor of the cloud has three eigendirections. The deformation of the cloud can be characterized by the rate of expansion or contraction along these eigendirections. Therefore, we consider two particles along an eigendirection with separation distance, x^* at any given time, t^*. The dynamics of each particle is governed by the Maxey–Riley equation [41] in one dimension, which is given

below:

$$m_p \frac{\mathrm{d}v^\star}{\mathrm{d}t^\star} = 3\pi\mu d_p(u^\star - v^\star) + m_f \frac{\mathrm{D}u^\star}{\mathrm{D}t^\star} + \frac{m_f}{2}\left(\frac{\mathrm{d}u^\star}{\mathrm{d}t^\star} - \frac{\mathrm{d}v^\star}{\mathrm{d}t^\star}\right), \tag{2.1}$$

where m_p and m_f are the masses of the particle and the displaced fluid, respectively, $u^\star$ is the dimensional fluid velocity at the particle location, $v^\star = \mathrm{d}x^*/\mathrm{d}t^*$ is the dimensional velocity of the particle, d_p is the particle diameter, and μ is the fluid viscosity. $\mathrm{D}/\mathrm{D}t^* = \partial/\partial t^* + u^*\partial/\partial x^*$ is the Lagrangian derivative along the trajectory of a fluid element. Similarly, $\mathrm{d}/\mathrm{d}t^* = \partial/\partial t^* + v^*\partial/\partial x^*$ is the Lagrangian derivative along particle trajectory. The first term on the right-hand side of Eq. (2.1), $3\pi\mu d_p\ (u^\star - v^\star)$ is the Stokes drag. The other two terms, i.e., $m_f\ \frac{\mathrm{D}u^\star}{\mathrm{D}t^\star}$ and $\frac{m_f}{2}\ (\frac{\mathrm{d}}{\mathrm{d}t^\star} - \frac{\mathrm{d}v^\star}{\mathrm{d}t^\star})$, which we call the pressure term and the added mass term arise due to the finite value of particle-to-fluid density ratio. Eq. (2.1) can be simplified to

$$\frac{\mathrm{d}v^\star}{\mathrm{d}t^\star} = \frac{6\pi\mu d_p}{(2m_p + m_f)}(u^\star - v^\star) + \frac{m_f}{(2m_p + m_f)}\left(2\frac{\mathrm{D}u^\star}{\mathrm{D}t^\star} + \frac{\mathrm{d}u^\star}{\mathrm{d}t^\star}\right). \tag{2.2}$$

The volume of each particle and the displaced fluid is $V = \pi d_p^3/6$. The particle density is ρ_p while the fluid density is ρ_f. We substitute $m_p = \rho_p V$ and $m_f = \rho_f V$ in Eq (2.2) to get

$$\frac{\mathrm{d}v^\star}{\mathrm{d}t^\star} = \frac{u^\star - v^\star}{\tau} + \frac{\beta}{3}\left(2\frac{\mathrm{D}u^\star}{\mathrm{D}t^\star} + \frac{\mathrm{d}u^\star}{\mathrm{d}t^\star}\right), \tag{2.3}$$

where $\beta = 3\rho_f/(2\rho_p + \rho_f)$ is the added mass factor and $\tau = (\rho_f + 2\rho_p)\ d_p^2/36\mu$ is the particle relaxation time. The time scale used to non-dimensionalize Eq. (2.3) is τ. To non-dimensionalize $u^\star$ and $v^\star$, we use d_p/τ. The non-dimensionalized form of Eq. (2.3) is given by

$$\ddot{x} = u - \dot{x} + \frac{\beta}{3}\left(2\frac{\mathrm{D}u}{\mathrm{D}t} + \frac{\mathrm{d}u}{\mathrm{d}t}\right), \tag{2.4}$$

where u, x and t are the non-dimensional terms corresponding to u^*, x^* and t^*.

As discussed before, RM was the first analytical study to be carried out on clustering where the main assumption was that the acceleration of the particles

is roughly the same as that of the background flow, or

$$\ddot{\boldsymbol{x}} = \frac{\mathrm{D}\boldsymbol{u}}{\mathrm{D}t}, \tag{2.5}$$

where $\boldsymbol{x}$ and $\boldsymbol{u}$ are vectors since RM analyzed the problem in three dimensions. It also assumed that the particle-to-fluid density ratio is infinite, or $\beta = 0$. The non-dimensionalized Maxey–Riley equation in three dimensions thus becomes

$$\ddot{\boldsymbol{x}} = \boldsymbol{u} - \dot{\boldsymbol{x}}. \tag{2.6}$$

Another assumption used in RM is $\overline{\nabla.\boldsymbol{u}} = 0$, where $\overline{(\bullet)}$ indicates the Lagrangian time-averaging along the trajectory of the particle. This means physically that the flow is assumed to be incompressible along the particle trajectory. Using these assumptions, we get

$$C := \overline{\nabla.\dot{\boldsymbol{x}}} = \overline{\nabla.\boldsymbol{u}} - \overline{\nabla.\ddot{\boldsymbol{x}}} = \overline{\nabla.\boldsymbol{u}} - \overline{\nabla.\left(\frac{\mathrm{D}\boldsymbol{u}}{\mathrm{D}t}\right)}, \tag{2.7}$$

where C is the rate of contraction or expansion of the cloud. We know that $\mathrm{D}/\mathrm{D}t = \partial/\partial t + \boldsymbol{u}.\nabla$ is the Lagrangian derivative along the trajectory of a fluid element. We also know that $\overline{\nabla.\boldsymbol{u}} = 0$. Hence, Eq. (2.7) simplifies to

$$C := -\frac{\partial\overline{(\nabla.\boldsymbol{u})}}{\partial t} - \overline{\nabla.(\boldsymbol{u}.\nabla\boldsymbol{u})}. \tag{2.8}$$

We neglect the ∇^2 term obtained from the simplification of Eq. (2.8) since the flow field is linear. We use the assumption $\overline{\nabla.\boldsymbol{u}} = 0$ again to get

$$C := -\overline{\frac{\partial u_i}{\partial x_j}\frac{\partial u_j}{\partial x_i}} = -\overline{||\Omega||^2 - ||S||^2} = Q, \tag{2.9}$$

where Ω and S are the dimensionless rotation-rate and strain-rate tensors respectively, and Q is half of the Q-criterion defined in [34, 35] used to identify vortical regions. $Q > 0$ and $Q < 0$ indicates the dominance of rotation-rate and strain-rate respectively. According to Eq. (2.9), the amount of clustering or dispersion, C, is linearly related to Q. $C > 0$ indicates dispersion, when particles

move away from each other over time, whereas for $C < 0$, the reverse happens and it is called clustering. The drawback of RM stems from its central assumption that the acceleration of the particles is the same as that of the background flow, which restricts the accuracy of RM to small Stokes number.

For turbulent flows, the Kolmogorov time scale, τ_η is often used as the flow time scale and is given by

$$\tau_\eta = \left(\frac{\nu}{\epsilon}\right)^{1/2}, \tag{2.10}$$

where ν is the kinematic viscosity, and ϵ is the average rate of dissipation of turbulence kinetic energy per unit mass of the fluid. Similarly, the Kolmogorov length scale, η is used as the corresponding flow length scale, where η is given by

$$\eta = \left(\frac{\nu^3}{\epsilon}\right)^{1/4}. \tag{2.11}$$

Eliminating ϵ from Eqs. (2.10) and (2.11) we get

$$\tau_\eta = \frac{\eta^2}{\nu}. \tag{2.12}$$

The kinematic viscosity, ν is related to the dynamic viscosity, μ as $\nu = \mu/\rho_f$. The Stokes number, St which characterizes the inertia of the particles is the ratio of the particle relaxation time and the Kolmogorov time scale, τ_η. So we have

$$\mathrm{St} := \frac{\tau}{\tau_\eta} = \frac{(\rho_f + 2\rho_p)\, d_p^2\, \nu}{36\mu\, \eta^2} = \frac{1}{18}\left(\frac{\rho_p}{\rho_f} + \frac{1}{2}\right)\left(\frac{d_p}{\eta}\right)^2. \tag{2.13}$$

Since we are interested in the Batchelor regime where $d_p < \eta$, we have an upper bound on the range of Stokes numbers where our analysis is valid; $\mathrm{St} < (\rho_p/\rho_f + 1/2)/18$. The smaller the density ratio, the lesser the upper bound on the Stokes number is. We will analyze the clustering of heavy particles ($\beta < 1$) in turbulence using these ideas later in Section 2.3.4.

In this chapter, we first derive a closed-form solution for the degree of clustering or dispersion from Eq. (2.1). Then, we will try to derive some key insights on the particle dynamics for different values of density ratios and Stokes number. Finally, we study the effect of the Basset term on clustering, which arise due to the boundary layer on the particles.

2.2 Analytical Derivation

We consider four particles at positions $\boldsymbol{X}$ and $\boldsymbol{X}+\delta\boldsymbol{X}^i$, with $i = 1, 2, 3$ at $t = 0$ as shown in Figure 1. These four particles constitute a cloud, the volume of which changes with time. We assume that the velocity field of the fluid is linear. Even if the flow is chaotic, the particles are smaller than the Kolmogorov length scale. The trajectory of a particle initially located at $\boldsymbol{X} + \delta\boldsymbol{X}$ is given by

$$x_i(\boldsymbol{X} + \delta\boldsymbol{X}, t) = x_i(\boldsymbol{X}, t) + \frac{\partial x_i}{\partial X_j}\delta X_j. \tag{2.14}$$

The kinematics of the cloud is fully characterized by Eq. (2.14) and the linear deformation tensor, J_{ij} such that: $J_{ij} = \frac{\partial x_i}{\partial X_j}$. The size of the cloud, in 3D is characterized by its volume, which is denoted by $V(t)$ and given by

$$V(t) = \det(x_i(\boldsymbol{X} + \delta\boldsymbol{X}^j, t) - x_i(\boldsymbol{X}, t)). \tag{2.15}$$

Clearly, $V(0) = det(\delta X_i^j)$. We are interested in finding out $V(t)/V(0)$ which is a measure of the change of the volume of the cloud. We use Eq. (2.14), Eq. (2.15) and the definition of $\boldsymbol{J}$ to express $V(t)/V(0)$ in terms of $\boldsymbol{J}$:

$$V(t)/V(0) = \det(\boldsymbol{J}(t)). \tag{2.16}$$

We define the finite time exponential rate of change of the volume, C^t as

$$V(t)/V(0) = \exp(C^t t). \tag{2.17}$$

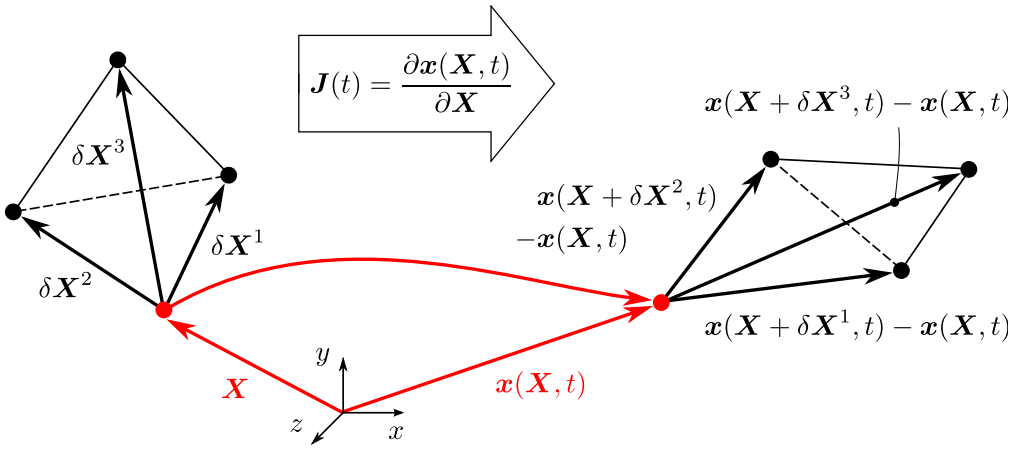

Figure 2.1: Schematic of a cloud of four particle as it moves from $\boldsymbol{X}$ and $\boldsymbol{X} + \delta X^j$, $j = 1, 2, 3$ at $t = 0$ to $\boldsymbol{x}(\boldsymbol{X}, t)$ and $\boldsymbol{x}(\boldsymbol{X} + \delta \boldsymbol{X}^j, t)$ at a given time. The relative motion is characterized by the tensor $\boldsymbol{J}$.

Combining Eq. (2.16) and Eq. (2.17), we get

$$C^t = \frac{1}{t} \ln[\det(\boldsymbol{J}(t))]. \tag{2.18}$$

At $t \to \infty$, it can be shown that $C^t \to C$, [1] which was defined earlier in Eq. (2.9). From a Lagrangian point of view, C is the exponential rate of change of volume after a sufficiently long time. As discussed before, if real $(C) > 0$, then the phenomenon is called dispersion and the size of the particle cloud increases with time. If real $(C) < 0$, then the size decreases with time and the particles come closer, which is known as clustering. C can be complex, where the imaginary part indicates that one of the particles of the tetrahedron shown in Figure 1 has crossed the plane formed by the other three. We call this phenomenon particle crossover.

There is a velocity gradient tensor associated with the cloud, and this tensor has three eigenvectors. These eigenvectors are directions along which the particle cloud experiences pure expansion or contraction. We assume that the rate of expansion or contraction of the cloud is the same in each direction. Hence

instead of analyzing the whole cloud, we shift our focus to a pair of particles on one of these directions and see if the distance between them increases or decreases over time. Hence, the 3D problem can be transformed into three identically similar independent 1D problems. In 1D, Eq. (2.4) becomes

$$\ddot{x} = u - \dot{x} + \beta\frac{\partial u}{\partial t} + \frac{\beta}{3}\left(2u\frac{\partial u}{\partial x} + \dot{x}\frac{\partial u}{\partial x}\right). \tag{2.19}$$

Differentiating Eq. (2.19) by X on both sides, we get

$$\ddot{J} = \frac{\partial u}{\partial x}J - \dot{J} + \beta\frac{\partial^2 u}{\partial t\partial x}J + \frac{1}{3}\beta\frac{\partial u}{\partial x}\left(2\frac{\partial u}{\partial x}J + \dot{J}\right) + \frac{1}{3}\beta\left(2u + \dot{x}\right)\frac{\partial^2 u}{\partial x^2}J, \tag{2.20}$$

where J=$\partial x/\partial X$. $\boldsymbol{J}$ is a second order tensor in 3D and becomes a scalar in 1D. The volume of the cloud at any time compared to the initial volume was given by det ($\boldsymbol{J}$) in 3D. In 1D, $J(t)$ equals the ratio of the distance between two particles at any given time and their initial separation distance. Now, $\partial u/\partial X = (\partial u/\partial x)(\partial x/\partial X)$ or $\partial u/\partial X = (\partial u/\partial x)\,J$ by chain rule. Also, $\partial^2 u/\partial x^2 = 0$ since the velocity field is linear. Eq. (2.20) thus becomes

$$\ddot{J} = \frac{\partial u}{\partial x}J - \dot{J} + \beta\frac{\partial^2 u}{\partial t\partial x}J + \frac{1}{3}\beta\frac{\partial u}{\partial x}\left(2\frac{\partial u}{\partial x}J + \dot{J}\right). \tag{2.21}$$

The rate of expansion or contraction along any eigendirection is known as the Lyapunov exponent, λ. Since we have transformed the initial problem into n independent 1D problems, the exponential rate of change of the cloud size, C, is related to λ by the relation:

$$C = n\lambda, \tag{2.22}$$

where n is the number of spatial dimensions in the problem. Eq. (2.18) in 1D then can be rewritten as $\lambda^t = \frac{1}{t}\ln(J(t))$ and $\lambda^t \to \lambda$ as $t \to \infty$. Since $\partial u/\partial x$ is a function of time, Eq. (2.21) is not a constant coefficient ordinary differential equation. To circumvent this problem, we use $F = \dot{J}/J$ where F is the rate of change of volume normalized by the volume of the cloud in 3D. The 1D analogy

would be the rate of change of distance between two particles normalized by the distance between the two particles. Since $FJ = \dot{J}$, we get

$$F\dot{J} + \dot{F}J = \ddot{J}, \tag{2.23}$$

or $F^2J + \dot{F}J = \ddot{J}$. Substituting for $\dot{J}$ and $\ddot{J}$ in Eq. (2.21), we get

$$\dot{F} + F^2 + F = \frac{\partial u}{\partial x} + \beta\frac{\partial}{\partial t}\left(\frac{\partial u}{\partial x}\right) + \frac{1}{3}\beta\frac{\partial u}{\partial x}\left(2\frac{\partial u}{\partial x} + F\right). \tag{2.24}$$

To proceed further, we recall the assumption that the velocity field of the background flow is linear in space, which means that the velocity gradient is a function of time alone (and not space), therefore we can represent it as a set of harmonic functions using Fourier transformation. So, the velocity gradient can be represented as:

$$\frac{\partial u}{\partial x} = \sum_{\omega} G(\omega)e^{i\omega t}, \tag{2.25}$$

where

$$G(\omega) = \frac{1}{2\pi}\int_{-\infty}^{\infty} \nabla u(t)e^{-i\omega t}dt. \tag{2.26}$$

Here, ω varies from $-\infty$ to ∞ and $\omega = 2\pi k/T$ where $k \in \mathbb{Z}$ and $T \to \infty$ is the sampling period. Further, we express F as follows:

$$F = \lambda + \sum_{\omega} \psi(\omega)e^{i\omega t}. \tag{2.27}$$

At long times, the rate of change of the distance normalized by the initial distance becomes constant, and is equal to the Lyapunov exponent, λ. $\psi(\omega)$ is the response of F to G, and is separated from the steady response, λ. Substituting for F and the velocity gradient in Eq. (2.24), we get

$$\begin{aligned}\lambda^2 + \lambda + \sum_{\omega}\left[(1 + 2\lambda + i\omega)\psi(\omega) - (1 + \frac{1}{3}\beta\lambda + i\beta\omega)G(\omega)\right]e^{i\omega t} \\ + \sum_{\omega}\sum_{\omega'}\left[\psi(\omega)\psi(\omega') - \frac{2}{3}\beta G(\omega)G(\omega') - \frac{1}{3}\beta G(\omega)\psi(\omega')\right]e^{i(\omega+\omega')t} = 0.\end{aligned} \tag{2.28}$$

The higher-order terms (beyond $e^{i\omega t}$) can be neglected. Also, $\psi(\omega)$ and $\psi(\omega')$ are only correlated when $\omega = -\omega'$. The same holds for $G(\omega)$ $G(\omega')$, and $G(\omega)$ $\psi(\omega')$ and Eq. (2.28) thus becomes

$$\begin{aligned}\lambda^2 + \lambda + \sum_{\omega}\left[(1 + 2\lambda + i\omega)\psi(\omega) - (1 + \frac{1}{3}\beta\lambda + i\beta\omega)G(\omega)\right]e^{i\omega t} \\ + \sum_{\omega}\left[\psi(\omega)\psi(-\omega) - \frac{2}{3}\beta G(\omega)G(-\omega) - \frac{1}{3}\beta G(\omega)\psi(-\omega)\right] = 0.\end{aligned} \tag{2.29}$$

For Eq. (2.29) to be true,

$$\lambda^2 + \lambda + \sum_{\omega}\psi(\omega)\psi(-\omega) = \frac{1}{3}\beta\sum_{\omega}G(\omega)\left[2G(-\omega) + \psi(-\omega)\right], \tag{2.30}$$

and

$$\psi(\omega) = (1 + 2\lambda + i\omega)^{-1}(1 + \frac{1}{3}\beta\lambda + i\beta\omega)G(\omega). \tag{2.31}$$

From Eq. (2.30) and Eq. (2.31), we get

$$\lambda^2 + \lambda + \sum_{\omega}\left(\frac{(1 + \beta\lambda/3)^2 + (\beta\omega)^2}{(1 + 2\lambda)^2 + \omega^2} - \frac{1}{3}\frac{\beta(1 + 2\lambda)(1 + \beta\lambda/3) + (\beta\omega)^2}{(1 + 2\lambda)^2 + \omega^2} - \frac{2}{3}\beta\right)G(\omega)G(-\omega) = 0. \tag{2.32}$$

Using the convolution theorem, the summation term can be expressed as a continuous integral. Eq. (2.32) then becomes

$$\lambda^2 + \lambda - \int_{-\infty}^{\infty}\frac{1}{9}\left(\frac{(3 - \beta\lambda - \beta)(3 + \beta\lambda) + 6(\beta\omega)^2}{(1 + 2\lambda)^2 + \omega^2} - 6\beta\right)\tilde{\rho}_Q d\omega = 0, \tag{2.33}$$

where $\tilde{\rho_Q}$ in 1D is defined as follows:

$$\tilde{\rho_Q} = -\frac{1}{2\pi}\int_{-\infty}^{\infty}\overline{\frac{\partial u(t')}{\partial x}\frac{\partial u(t + t')}{\partial x}}e^{-i\omega t}dt. \tag{2.34}$$

Extending Eq. (2.33) to n dimensions, we get

$$\lambda^2 + \lambda - \frac{1}{n}\int_{-\infty}^{\infty}\frac{1}{9}\left(\frac{(3 - \beta\lambda - \beta)(3 + \beta\lambda) + 6(\beta\omega)^2}{(1 + 2\lambda)^2 + \omega^2} - 6\beta\right)\tilde{\rho}_Q d\omega = 0. \tag{2.35}$$

Eq. (2.35) is an integral equation. To evaluate the integral, we need to know the value of λ, which is the solution itself. Hence further simplification of the

integral is required, as discussed in Section 2.3. We note that RM is a special form of Eq. (2.35) when $|\lambda| << 1$, $\beta = 0$ and $\omega \approx 0$ since it is valid only for small values of Stokes number and infinite density ratio. The integral in Eq. (2.35) for RM reduces to $\overline{||\Omega||^2 - ||S||^2}$, which is the same as Eq. (2.9). A change in time scale would affect ω, λ and $\tilde{\rho_Q}$, thereby changing the equation above. For example, instead of the particle relaxation time, we can choose the Kolmogorov time scale as the time scale for the analysis, the details of which are provided in Section 2.3.4.

2.3 One Dimensional Unimodal Excitation

We consider a 1D problem with the background flow having a single frequency. IDR shows that this simple 1D model accurately predicts much of the clustering phenomenon in turbulence. We use this model for the more general case of finite particle-to-fluid density ratio. Later on, we show that this 1D problem can be also used for flows in higher dimensions. For the 1D flow, the velocity gradient is defined as:

$$\frac{\partial u}{\partial x} = \sqrt{-2\phi}\, cos(\omega t). \tag{2.36}$$

The factor of -2 and the square root have been used to allow for a one-to-one correspondence between $\tilde{\rho_Q}$ and ϕ. u is the background flow around the particles located on the x-axis. ϕ can take complex values, the meaning of which will be discussed later. For now, we assume that ϕ is real. When $\phi < 0$, the velocity gradient coefficient, i.e $\sqrt{-2\phi}$, is real. This represents straining flow since u is of the form: $u = Axcos(\omega t)$, which means that u is real and the particles move towards or away along a line. $\phi > 0$ however is not easy to visualize in 1D. One

can imagine the line to have a rotational motion with the particles moving along concentric arcs. We henceforth call it the rotating regime. The velocity gradient, in this case, is purely imaginary.

If we imagine two particles separated by Δx, the difference in velocities between them is Δu, where $\Delta u = (\partial u/\partial x)\Delta x$. Since u is a linear function of x, $(\partial u/\partial x)$ is independent of Δx. Δu or the rate of change of separation between the particles at that instant scales with the separation distance, Δx. Hence, the separation distance varies exponentially with time, and we define the Lyapunov exponent, λ, as the exponential rate at which the particles converge towards or diverge away from each other.

We proceed by simplifying Eq. (2.35). The canonical flow model has one single frequency, say ω'. Hence we have

$$\tilde{\rho_Q}(\omega') = n\phi\delta(\omega - \omega'). \tag{2.37}$$

From Eq. (2.35) and Eq. (2.37), we get:

$$\lambda^2 + \lambda - \frac{1}{9}\left(\frac{(3-\beta\lambda-\beta)(3+\beta\lambda) + 6(\beta\omega)^2}{(1+2\lambda)^2+\omega^2} - 6\beta\right)\phi = 0. \tag{2.38}$$

Let $\gamma = 1 + 2\lambda$, which means that $\lambda = \frac{\gamma-1}{2}$. Substituting for λ, Eq. (2.38) becomes

$$\gamma^4 - 2k\gamma^2 - l = 0, \tag{2.39}$$

where $k = \frac{1-\omega^2}{2} - \frac{1}{18}(24+\beta)\beta\phi$ and $l = \omega^2 + \frac{1}{9}\left[(6-\beta)^2 + 24(\beta-1)\beta\omega^2\right]\phi$. This is a second-order polynomial equation in γ^2, the solution for which is

$$\gamma^2 = k \pm \sqrt{k^2 + l}. \tag{2.40}$$

When there is no flow ($\phi = 0$), there should not be any clustering or dispersion, which means $\lambda = 0$ or $\gamma = 1$. This condition eliminates one solution for γ^2.

Imposing the condition $\lambda = 0$ or $\gamma = 1$ at $\phi = 0$ again we get

$$\lambda = -\frac{1}{2} + \frac{1}{2}\sqrt{k + \sqrt{k^2 + l}}. \tag{2.41}$$

Eq. (2.41) is a closed-form solution for the Lyapunov exponent. We observe the following from Eq. (2.41):

1. The Lyapunov exponent, λ, depends on the oscillation amplitude, ϕ, the added mass factor, β, and the oscillation frequency, ω. The real part of the exponent signifies expansion or contraction. real(λ) < 0 implies clustering, where the distance between two particles decreases with time, whereas real(λ) > 0 implies dispersion, where the separation distance increases.

2. A non-zero value of imag (λ) indicates particle crossover, when the tetrahedral cloud collapses and flips. In the one-dimensional setting, imag(λ) $\neq 0$ implies that the two particles have exchanged sides on the line.

3. Since the last term in Eq. (2.41) is always positive, the Lyapunov exponent has a lower bound of $-1/2$ regardless of the particle-to-fluid density ratio. There is no upper bound on the Lyapunov exponent. In other words, there is a limit on how quickly the particles can come close to one another, but particles can move away from one another unbounded.

4. All the equations derived so far are normalized by τ. Such a normalization restricts the analysis to particles with the same diameter. In reality, we encounter particles with different diameters in the same flow. To ensure that we can carry out the analysis for all of them simultaneously, we normalize the results by the Kolmogorov time-scale or the flow time scale, τ_η, instead. We employ the subscript η to distinguish parameters that are normalized by τ_η. Thus we have $\lambda = \mathrm{St}\ \lambda_\eta$, $\omega = \mathrm{St}\ \omega_\eta$, and $\phi = \mathrm{St}^2\ \phi_\eta$. Since ϕ_η

remains the same for all the particles, a larger Stokes number corresponds to a larger ϕ.

5. The parameter β is a function of the particle-to-fluid density ratio and varies as $\beta = 3/(2\rho_p/\rho_f + 1)$. Therefore, when the particle is lighter than the fluid, $\beta > 1$. For particles heavier than the fluid, $\beta < 1$. Special cases include very heavy particles ($\rho_p >> \rho_f$) with $\beta = 0$, neutrally buoyant particles ($\rho_p = \rho_f$) with $\beta = 1$, and very light particles ($\rho_p << \rho_f$) with $\beta = 3$. Similarly, $\phi > 0$ and $\phi < 0$ indicate the rotating and straining regimes, respectively.

6. In the rotating regime, λ can never be complex if $\omega < 5.5/\sqrt{(6)} \approx 2.25$. Beyond this limit, the higher the value of ω, the smaller is the value of ϕ at which λ becomes complex.Therefore, particle crossover does not take place in the rotating regime unless ϕ or ω is very large.

7. $\lambda = 0$ for $\beta = 1$ unless $\phi < -9(1 + \omega^2)/25$. In other words, neutrally buoyant particles perfectly mimic the background flow, provided that the flow is not highly straining or oscillating. Similarly, $\lambda = 0$ for $\phi = 0$ or no-flow. This in fact is a condition which we used while deriving the closed-form solution for λ.

8. Finally, particle crossover takes place when either $\sqrt{k + \sqrt{k^2 + l}} < 0$ or $\sqrt{k^2 + l} < 0$. For chaotic flows, $\omega \approx 0$, it can be shown that particle crossover only takes place for dense particles in a straining flow.

2.3.1 Agreement of the present analysis with IDR and RM

Our present analysis is a more general form of IDR and RM. IDR assumes that the particle-to-fluid density ratio is infinite, or in other words $\rho_p/\rho_f \to \infty$ or $\beta = 0$. So Eq. (2.41) in our analysis reduces to:

$$\lambda = -\frac{1}{2} + \frac{1}{4}\sqrt{2(1-\omega^2) + 2\sqrt{(1+\omega)^2 + 16\phi}}\,. \tag{2.42}$$

Similarly, Eq (2.35), which relates clustering or dispersion to $\tilde{\rho_Q}$, reduces to:

$$\lambda^2 + \lambda - \frac{1}{n}\int_{-\infty}^{\infty} \frac{\tilde{\rho_Q}}{(1+2\lambda)^2 + \omega^2} d\omega = 0. \tag{2.43}$$

Eqs. (2.42) and (2.43) had been proved in IDR, hence there is an agreement with our analysis when the density ratio goes to infinity and the analysis in IDR.

Similarly, the central assumption in RM is that the particle acceleration is roughly equal to the fluid acceleration. Like IDR, RM also assumes that $\beta = 0$. We have used these assumptions to derive Eq. (2.9). We also use Eqs. (2.22) and (2.37) to show that RM can be simplified as follows:

$$\lambda = \phi. \tag{2.44}$$

In our analysis, Eq. (2.41) at the limits of $\phi << 1$ and $\omega \approx 0$ becomes the same as Eq. (2.44).

Thus, to summarize, in our analysis we obtain the Lyapunov exponent, λ, as a function of β, ϕ, and ω. It agrees with the result obtained in IDR at the limit of infinite density ratio, and with the result in RM at small values of ϕ.

2.3.2 Numerical Validation

The rate of clustering or dispersion at long times is related to x as $C = \lim_{t\to\infty} ln\ [x(t+T)/x(t)]$. Hence, one way to numerically validate our results is to compute the ratio $x(t+T)/x(t)$ from Eqs. (2.4) and (2.36) as $t \to \infty$, where T is the period of oscillation. However, x grows exponentially with time, leading to an ill-conditioned system. To avoid this problem, instead of the brute-force approach, we solve the eigenvalue problem for one cycle. This method also avoids the large computational error incurred otherwise.

For the 1D canonical flow discussed above, $\partial u/\partial x$ is a harmonic function with period T. Let us now define a 2×2 transformation matrix, A, which satisfies:

$$\begin{bmatrix} x(T) \\ v(T) \end{bmatrix} = A \begin{bmatrix} x(0) \\ v(0) \end{bmatrix}. \tag{2.45}$$

For the 1D modal problem, we select 2 linearly independent initial conditions for $[x\ \ v]^T$, and the time evolution is calculated based on Eq. (2.4) in each case. A good choice for $[x(0)\ \ v(0)]^T$ is $[1\ \ 0]^T$ and $[0\ \ 1]^T$ respectively. Evaluating $[x(T)\ \ v(T)]^T$ twice gives us both columns, and hence, the matrix A. A has two eigenvalues, which correspond to how $[x\ \ v]^T$ changes after one cycle compared to the initial value. Only the eigenvalue with the larger magnitude is important, since the other one decays at long times. This is the Lyapunov exponent that we have already analytically derived before. We have used the second-order Adams–Bashforth method to evaluate how $[x\ \ v]^T$ evolves in time using the Maxey–Riley Equation. The time step that we have used is $1 \times 10^{-5}\pi/\omega$, and it produces sufficiently small errors.

In this study, particle dynamics depends on three parameters in the strain-

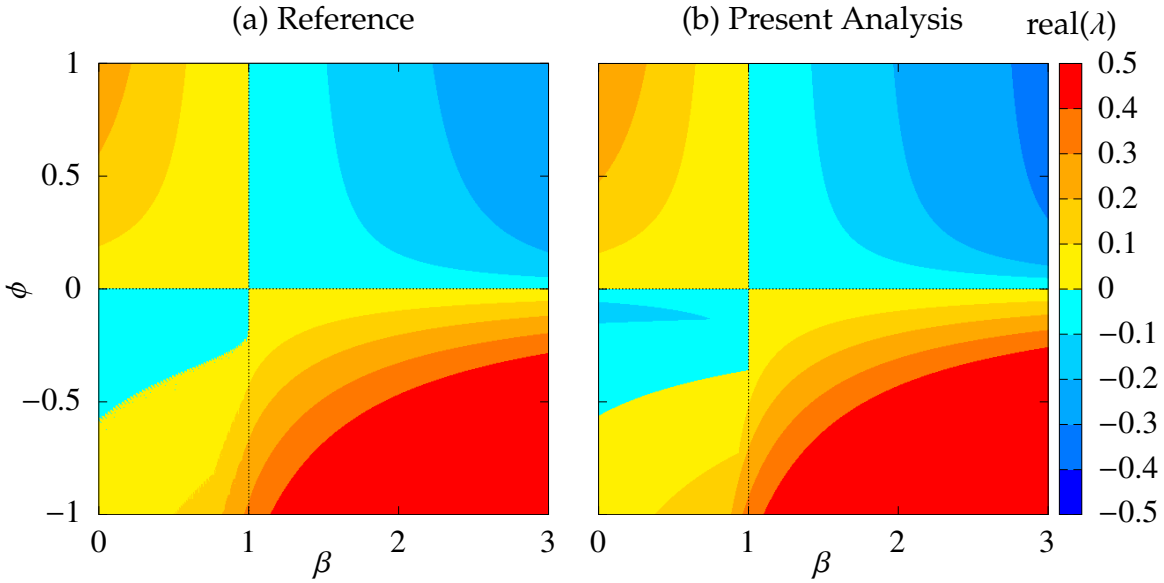

Figure 2.2: The rate of contraction or expansion, real (λ) obtained (a) numerically and (b) analytically as a function of the oscillation amplitude, ϕ and the added mass factor, β. The oscillation frequency is assumed to be very small ($\omega \approx 0$).

ing and rotating regimes, namely the velocity gradient, $\sqrt{-2\phi}$, the frequency of oscillation, ω, and the added mass factor, β. To get a better understanding, we let one of the parameters be constant and see how the rate of expansion or contraction varies as a function of the other two parameters obtained using both the numerical technique discussed above and the analytical derivation, Eq. (2.41). In Figure 2.2, the frequency of oscillation is kept very small ($\omega = 0.01$) so that any further decrease in ω would not affect the results. Our entire domain is divided into four subdomains where $\beta < 1$ and $\beta > 1$ indicate heavy and light particles, respectively. Similarly, $\phi < 0$ and $\phi > 0$ indicate the straining and rotating regime, respectively. We observe that in the rotating regime ($\phi > 0$), only dispersion is observed for heavy particles ($\beta < 1$), and only clustering is observed for lighter particles ($\beta > 1$). This is intuitive since in rotating flows, heavy particles tend to move away and light particles move towards the center of rotation. In the straining regime ($\phi < 0$), there can be clustering or dispersion for heavy particles depending on the velocity gradient and the added mass factor. For neutrally buoyant particles ($\beta = 1$), we observe that beyond a certain

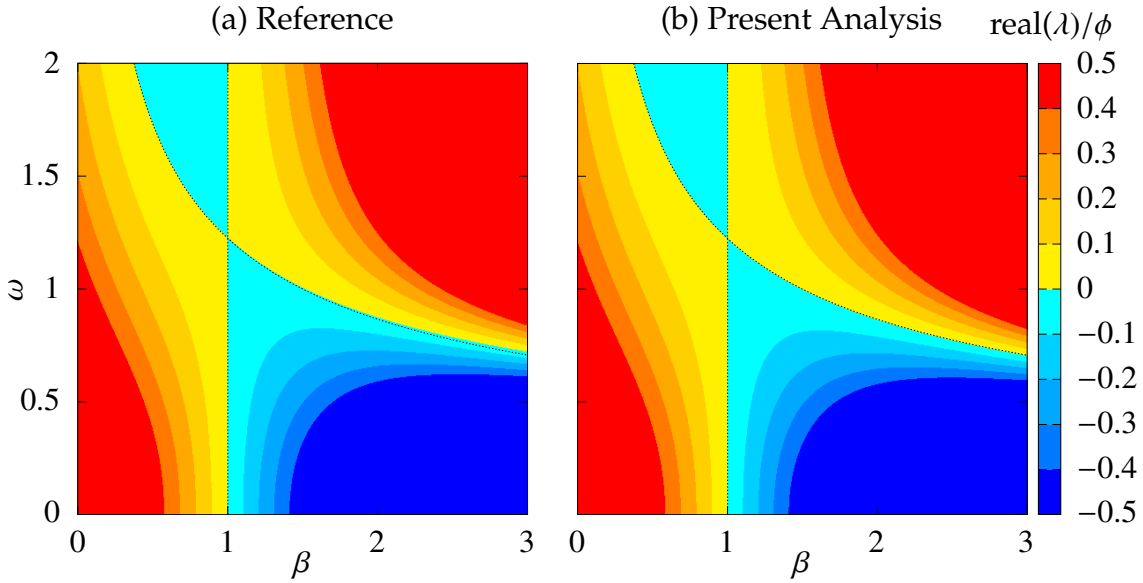

Figure 2.3: The rate of contraction or expansion, real (λ) normalized by the oscillation amplitude, ϕ as a function of the added mass factor, β and the oscillation frequency, ω obtained (a) using numerical integration and (b) analytical prediction. ϕ is assumed to be very small ($\phi \approx 0$).

ϕ in the straining regime, particle dispersion takes place as predicted. For light particles, only dispersion is observed in the straining regime.

In Figure 2.3, ϕ is considered to be very small (ϕ <<1) and the Lyapunov exponent normalized by ϕ is evaluated as a function of the added mass factor and the frequency of oscillation. For $\phi \approx 0$, Eq. (2.41) can be expressed as a linear function of ϕ by the following expression:

$$\frac{\lambda}{\phi} = (1-\beta)\frac{(1-\frac{2}{3}\beta\omega^2)}{1+\omega^2}. \tag{2.46}$$

From Eq. (2.46), we infer that the Lyapunov exponent can be zero when either the added mass factor, β is unity, or when $\omega^2 = 3/2\beta$. This means that for neutrally buoyant particles and the curve $\omega^2 = 3/2\beta$, there is no clustering and dispersion. We can see in Figure 2.3 that the dashed curve ($\omega^2 = 3/2\beta$) and the line $\beta = 1$ demarcate the clustering and dispersion regimes. For dense particles, we observe dispersion at smaller frequencies and clustering beyond the $\omega^2 = 3/2\beta$ curve. For light particles, the opposite is observed. Overall, there is a

very good match between the analytical and numerical results.

2.3.3 Implication on 3D flows

Our earlier discussion assumed a single frequency of oscillation and a real value of ϕ for the background flow, as described in Eq. (2.36). The question that automatically follows is whether we can extend this 1D model to 3D flows. To answer this, we will use the same argument we used while deriving an expression for the Lyapunov exponent: particle clustering in 3D can be broken down into three identical but independent 1D problems. If we have a particle that is located in a particular eigendirection, it will not be influenced by the flow in the other two eigendirections. Our initial 1D formulation with real ϕ is not sufficient to describe 3D flows. We need to re-evaluate the domain of ϕ to make our formulation more generic. To help this discussion, we use the fact that the velocity gradient tensor, ∇u has three eigenvalues in 3D and two eigenvalues in 2D. In 2D, we denote the eigenvalues be λ_1^u and λ_2^u (the superscript u is used to distinguish it from the Lyapunov exponent). For 2D and 3D flows, the eigenvalues can be complex. Also, due to the continuity equation, the sum of the eigenvalues is zero. This is only possible when λ_1^u and λ_2^u are both real or are both imaginary, with one value being the opposite sign of the other. This means to characterize 2D flows, ϕ can now take both positive and negative real values. $\phi < 0$ characterizes straining flows, whereas $\phi > 0$ characterizes rotating flows, which we have already discussed.

For 3D flows, we denote the eigenvalues by λ_1^u, λ_2^u and λ_3^u. All the eigenvalues can be real in such a way that the sum is zero. However, there is a possibility

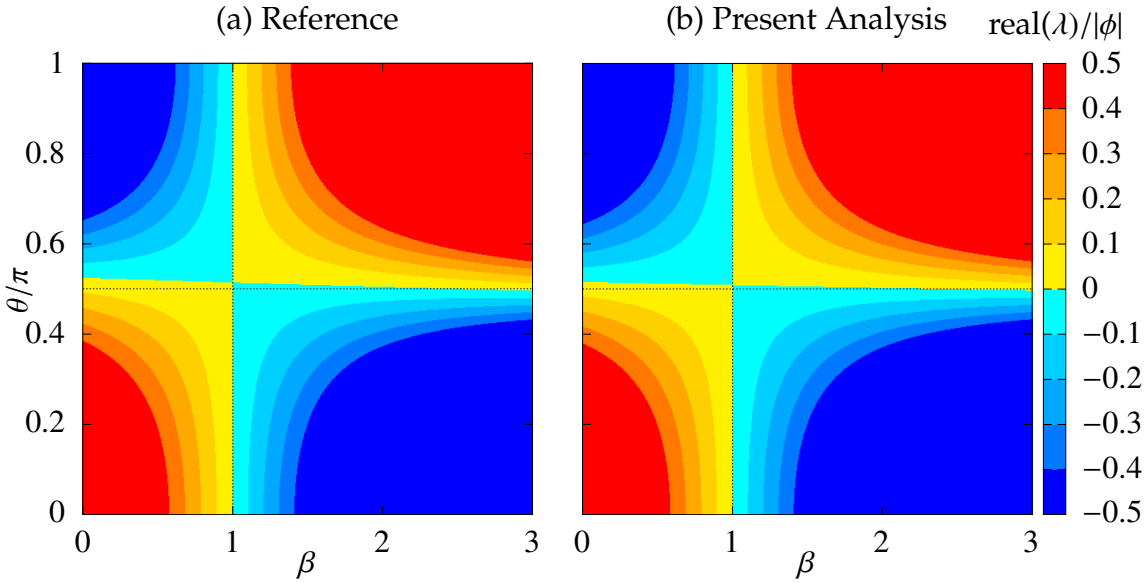

Figure 2.4: The rate of contraction or expansion, real (λ) normalized by the oscillation amplitude, $|\phi|$ as a function of the added mass factor, β and the oscillation amplitude phase angle, θ obtained (a) using numerical integration and (b) analytical prediction. Both $|\phi|$ and ω are assumed to be very small ($\phi \approx 0$) and ($\omega \approx 0$).

that there is a complex conjugate pair among the three. This means that we can have a pair of eigenvalues with both real and imaginary parts. For example if $\lambda_1^u = 2$, then $\lambda_2^u = -1 + i$ and $\lambda_3^u = -1 - i$. Therefore, to extend our 1D model to 3D we need to extend the domain of ϕ to include complex values. ϕ now has the form $\phi = |\phi|\, e^{i\theta}$ where θ is called the phase angle and can take any value between 0 to π for 3D flows and either 0 or π for 2D flows.

Physically, a non-zero value of θ implies that stretching (or contraction) and rotation are occurring simultaneously, an example unique only to 3D flows would be vortex stretching. The dynamics now depend on one more parameter, θ. Figure 2.4 shows the variation of the rate of expansion or contraction normalized by the oscillation amplitude (real(λ)/ϕ) as a function of the phase angle, θ, and the added mass factor, β, for small values of $|\phi|$ and ω. Analytically, for such cases, Eq (2.41) simplifies to

$$\frac{\text{real}\ (\lambda)}{|\phi|} = (1 - \beta)\cos(\theta). \tag{2.47}$$

For particles denser than the fluid, particles tend to disperse away as θ is small. This tendency decreases as the degree of rotation decreases and the degree of straining associated with the flow increases. In other words, θ increases for a given density ratio until particles begin to cluster. This transition takes place at $\theta = \pi/2$ as observed in Figure 2.4 and predicted in Eq. (2.47). When the value of θ is further increased, we notice an increase in clustering. Lighter particles, however, tend to cluster as θ is small. This tendency decreases as θ increases for a given β till particles begin to disperse at $\theta = \pi/2$. When the value of θ is further increased, we notice an increase in dispersion. There is no clustering for $\theta = \pi/2$ and $\beta = 1$. Overall, Figure 2.4 shows a good agreement between our analytical predictions in Eq. (2.41) and the numerical calculations. This shows that our 1D unimodal model can be extended to 3D flows.

2.3.4 Relevance of the 1D modal problem in predicting clustering for heavy particles ($\beta < 1$) in turbulence

The numerical results obtained so far use the Maxey–Riley equation normalized by τ or Eq. (2.4). To make the analysis more general to study particles of different sizes and densities in the same flow, we use τ_η or the flow time scale for normalization. We also revisit the argument that we made earlier that there is a one-to-one correspondence between our 1D model and 3D turbulence when $\omega_\eta \approx 0$. This is because one can argue that the frequency of oscillation is much smaller than the inverse of the particle relaxation time for chaotic flows. After renormalizing Eq. (2.41) with the flow scale, we get

$$\lambda_\eta = -\frac{1}{2\mathrm{St}} + \frac{1}{2\mathrm{St}}\sqrt{k' + \sqrt{k'^2 + l'}}, \tag{2.48}$$

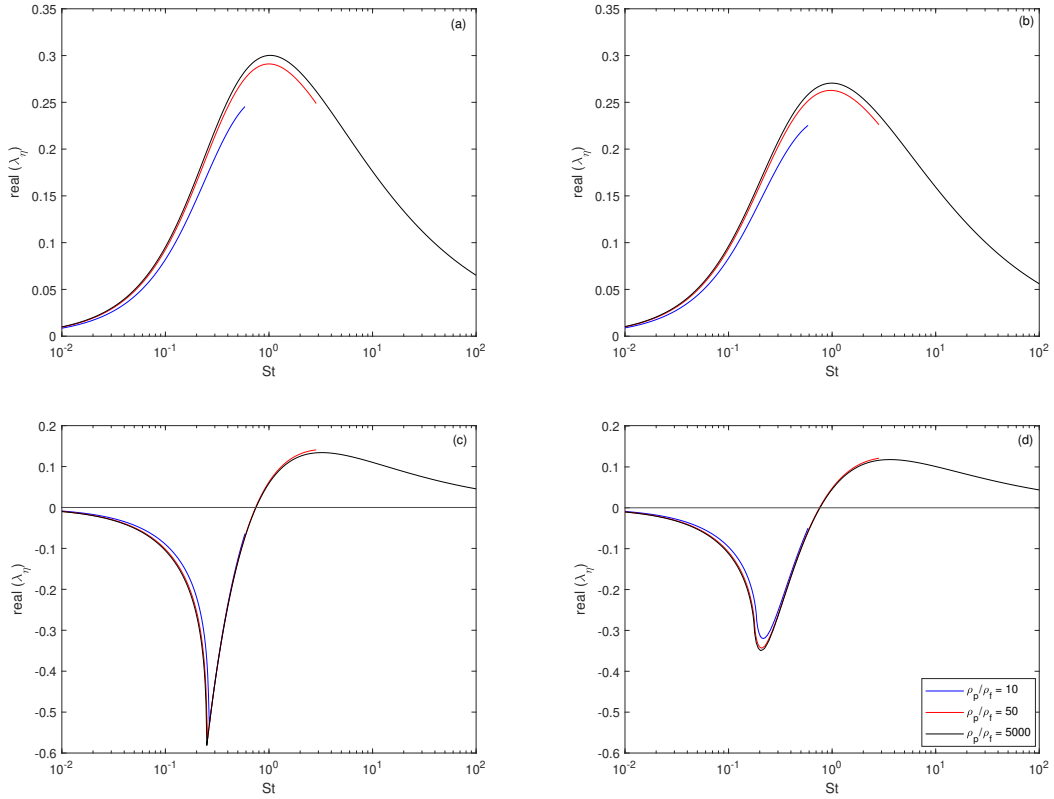

Figure 2.5: The rate of expansion or contraction, real (λ_η) as a function of the Stokes number from (a) the present analysis and (b) reference computational results in the rotating regime ($\phi_\eta = 1$) and from (c) the present analysis and (d) reference computational results in the straining regime ($\phi_\eta = -1$) for density ratios, $\rho_p/\rho_f = 10$ (blue), 50 (red) and 5000 (black).

where $k' = \frac{1}{2} - \frac{1}{18}(24 + \beta)\,\beta\phi_\eta\,St^2$ and $l' = \frac{1}{9}(6 - \beta)^2\phi_\eta St^2$. We see how the rate of clustering or dispersion varies as a function of the Stokes number obtained from the present analysis in Figure 2.5 (a) and the reference numerical results in Figures 2.5 (b) for three different density ratios. It validates the fact that there is negligible clustering at small and large values of the Stokes number.

Our analysis is valid up to a certain Stokes number, which we call the critical Stokes number, St_{cr}, beyond which the particle diameter is no longer smaller than the Kolmogorov length scale, η. For large density ratios, we can investigate both high and low values of Stokes numbers and show how the clustering

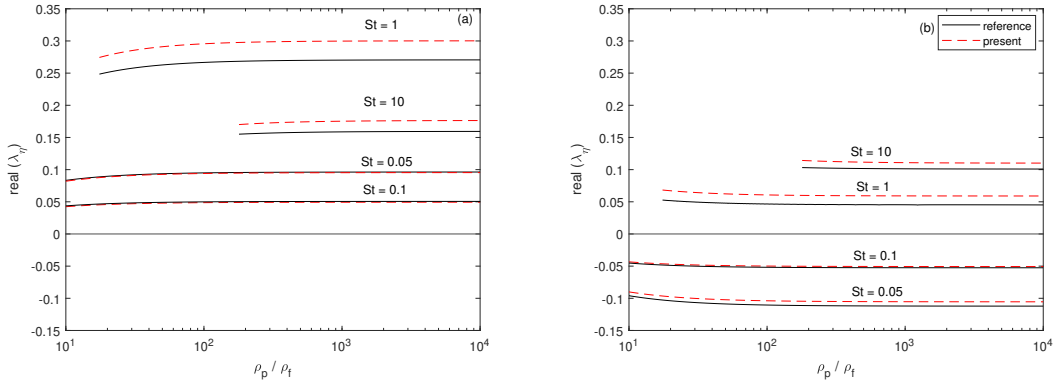

Figure 2.6: The rate of expansion or contraction, real (λ_η) as a function of the particle-to-fluid density ratio from the present analysis (red dashed) and reference numerical results (black solid) (a) in the rotating ($\phi_\eta = 1$) and (b) straining regime ($\phi_\eta = -1$) for different Stokes number.

phenomenon becomes negligible at both the limits. For smaller density ratios however, St_{cr} decrease (for example, for density ratio = 50, the value of this limit is 2.8). Therefore, we have restricted the analysis of this section to heavy particles only. St_{cr} is so small for light particles that we already know that clustering would be a linear function of the Stokes number.

Our analysis captures the non-monotonic behavior for finite density ratios. There is a good agreement between the present analysis and reference numerical results as illustrated in Figures 2.5 (a) and 2.5 (b). As we increase St from zero in the straining regime, real (λ_η) decreases monotonically till a minimum value. Real (λ_η) increases with a further increase in the Stokes number. RM failed to explain a lower bound on the real value of the Lyapunov exponent since, according to Eq (2.9), clustering is unbounded. With a further increase in the Stokes number, real (λ_η) become positive and particles begin to disperse. In the rotating regime, real (λ_η) is always greater than zero. This means clustering is not observed for any value of Stokes number in this regime. Both the present analysis and the reference numerical results predict the same trend for

finite density ratios.

The rate of clustering or dispersion as a function of particle-to-fluid density ratio (instead of β since we restrict this subsection to heavy particles in turbulence) is shown next for different Stokes numbers in the rotating regime in Figure 2.6 (a) and the straining regime in Figure 2.6 (b). For the rotating regime, we observe that an increase in density ratio leads to an increase in dispersion in the straining regime. This is because the outward force acting on the particles increases with an increase in the density ratio. There is no clustering in the rotating regime. This is obvious since we only consider particles whose density is greater than that of the fluid.

For the straining regime, an increase in the density of the particles leads to more clustering. This is intuitive since less dense particles have a greater tendency to act as neutral fluid tracers and hence, have a smaller value of clustering. However, an increase in the density ratio leads to a decrease in dispersion, which is counter-intuitive. We also note that as we increase the density ratio, the change in the Lyapunov constant becomes more gradual and eventually converges to the results predicted by IDR. This is because at higher density ratios, the added mass and the pressure terms in Eq. (2.1) become negligible and the only important force is the drag force.

2.3.5 Results for particles with negligible densities ($\beta \approx 3$) and neutrally buoyant particles ($\beta = 1$)

For neutrally buoyant particles, $\beta = 1$. Thus Eq. (2.41) simplifies to:

$$\lambda = -\frac{1}{2} + \frac{1}{2}\sqrt{\frac{(1-\omega^2)}{2} - \frac{25}{18}\phi + \sqrt{\left(\frac{(1+\omega^2)}{2} + \frac{25}{18}\phi\right)^2}}. \tag{2.49}$$

If the last term under the square root, i.e., $\frac{(1+\omega^2)}{2} + \frac{25}{18}\phi$ is greater than zero, then we end up with $\lambda = 0$, which is the intuitive result. In physical terms, it means that there is no clustering or dispersion for neutrally buoyant particles, which is expected. However, when

$$\frac{(1+\omega^2)}{2} + \frac{25}{18}\phi < 0 \tag{2.50}$$

or

$$\phi < -\frac{9(1+\omega^2)}{25}, \tag{2.51}$$

λ is no longer zero. This means that for strong straining flows, neutrally buoyant particles disperse. λ in that case is given by:

$$\lambda = -\frac{1}{2} + \frac{1}{2}\sqrt{-\left(\omega^2 + \frac{25}{9}\phi\right)}. \tag{2.52}$$

For very small frequencies ($\omega \approx 0$), $\lambda \neq 0$ only for $\phi < -9/25 \approx -0.36$. λ is approximately equal to $-\frac{1}{2} + \frac{5}{6}\sqrt{-\phi}$. Hence, there is no upper bound on the dispersion of such particles. We also observe that there is no way λ can be complex, hence particle crossover is not observed at all.

Next, we look at what happens for very light particles such that $\beta \approx 3$. Eq. (2.41) in this form is intractable and needs further simplification. Hence, we want to see what happens to such light particles in chaotic flows when $\omega \approx 0$.

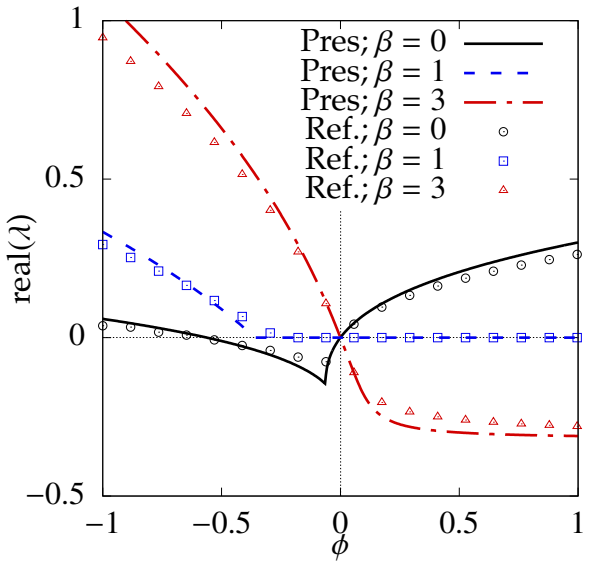

Figure 2.7: The rate of expansion or contraction, real (λ) as a function of the oscillation amplitude, ϕ at $\omega \approx 0$ for infinite density particles (black), neutrally buoyant particles (blue) and extremely light particles (red) obtained both from the analytical derivation (present analysis) and numerical integration (reference).

Under this additional approximation, we get,

$$\lambda = -\frac{1}{2} + \frac{\sqrt{(2)}}{4}\sqrt{1 - 9\phi + \sqrt{1 - 14\phi + 81\phi^2}}. \tag{2.53}$$

For light particles, the Lyapunov exponent is always greater than zero for straining flows and always less than zero for rotating flows. There is no particle crossover at all. Further, we observe that $\lambda = -2\phi$ for $|\phi| \approx 0$. Hence, clustering has a linear dependence on ϕ at very small oscillation amplitudes. If $|\phi| >> 1$, λ scales with $|\phi|^{1/2}$ in the straining regime and $|\phi|^{1/4}$ in the rotating regime. Figure 2.7 shows a very good match between the analytical prediction and the numerical results for neutrally buoyant ($\beta = 1$), very light ($\beta \approx 3$) and very dense particles ($\beta \approx 0$) and shows all the trends discussed in this subsection.

2.3.6 Inclusion of the Basset history term

The analysis so far had neglected the effect of the Basset history term, which physically represents the lagging boundary layer developed on the surface of the particle as it is subjected to the background flow. As the name suggests, this force term includes the effect of the particle and fluid flow acceleration at all instances in the past. The Maxey–Riley Equation with the history term is given by:

$$m_p \frac{\mathrm{d}v^\star}{\mathrm{d}t^\star} = 3\pi\mu d_p(u^\star - v^\star) + m_f \frac{\mathrm{D}u^\star}{\mathrm{D}t^\star} + \frac{m_f}{2}\left(\frac{\mathrm{d}u^\star}{\mathrm{d}t^\star} - \frac{\mathrm{d}v^\star}{\mathrm{d}t^\star}\right) + \frac{3\pi d_p^2 \mu}{2\sqrt{\pi\nu}} \int_0^{t^\star} \frac{g^\star(\tau)}{\sqrt{t^\star - \tau}} \mathrm{d}\tau, \quad (2.54)$$

where m_p and m_f are the masses of the particle and the displaced fluid respectively, $u^\star$ is the dimensional fluid velocity and $v^\star$ is the dimensional velocity of the particle, d_p is the particle diameter, and μ is the fluid viscosity. The integral term is the history force, where $g^\star(\tau) = \frac{\mathrm{d}}{\mathrm{d}\tau}(u^\star - v^\star)$. The Maxey–Riley equation assumes that the initial velocities of the particles as well as the background flow is zero. Accounting for the initial slip between the particles and the fluid, the Maxey–Riley equation gets modified [42, 43] as follows:

$$\begin{aligned} m_p \frac{\mathrm{d}v^\star}{\mathrm{d}t^\star} = 3\pi\mu d_p(u^\star - v^\star) + m_f \frac{\mathrm{D}u^\star}{\mathrm{D}t^\star} + \frac{m_f}{2}\left(\frac{\mathrm{d}u^\star}{\mathrm{d}t^\star} - \frac{\mathrm{d}v^\star}{\mathrm{d}t^\star}\right) + \\ \frac{3\pi d_p^2 \mu}{2\sqrt{\pi\nu}} \left(\int_0^{t^\star} \frac{g^\star(\tau)}{\sqrt{t^\star - \tau}} \mathrm{d}\tau + \frac{u^*(0) - v^*(0)}{\sqrt{t^*}} \right), \end{aligned} \quad (2.55)$$

where $v^*(0)$ and $u^*(0)$ are the particle and fluid velocities at $t = 0$. The history force includes the initial slip as well. The non-dimensionalized form of Eq. (2.55) is given by

$$\ddot{x} = u(x,t) - \dot{x} + \frac{\beta}{3}\left(2\frac{\mathrm{D}}{\mathrm{D}t}u(x,t) + \frac{\mathrm{d}}{\mathrm{d}t}u(x,t)\right) + \sqrt{\frac{3\beta}{\pi}}\left(\int_0^t \frac{g(\tau)}{\sqrt{t-\tau}}\mathrm{d}\tau + \frac{u(0) - v(0)}{\sqrt{t}}\right). \quad (2.56)$$

We use the same scales for non-dimensionalization as in Eq. (2.4) We call the integral term in Eq. (2.56) I_B. We want to see how the term behaves for the

clustering and the dispersion case. I_B is an improper integral given by:

$$I_B(t) = \int_0^t \frac{g(\tau)}{\sqrt{t-\tau}} \mathrm{d}\tau. \tag{2.57}$$

T is the time period of oscillation associated with the unimodal excitation of the background flow. Expressing this integral as a sum of the first cycle's effect and the rest, we get

$$I_B(t) = \int_0^T \frac{g(\tau)}{\sqrt{t-\tau}} \mathrm{d}\tau + \int_T^t \frac{g(\tau)}{\sqrt{t-\tau}} \mathrm{d}\tau. \tag{2.58}$$

Applying the substitution method on the second integral, we obtain

$$I_B(t) = \int_0^T \frac{g(\tau)}{\sqrt{t-\tau}} \mathrm{d}\tau + \int_0^{t-T} \frac{g(\tau+T)}{\sqrt{(t-T)-\tau}} \mathrm{d}\tau. \tag{2.59}$$

We assume that u and v vary exponentially, as they do in the absence of the history term. Hence, the ratio of $g(\tau+T)/g(\tau)$, which we call the displacement ratio, k has a constant value, at very long times. Thus, we get

$$I_B(t) = \int_0^T \frac{g(\tau)}{\sqrt{t-\tau}} \mathrm{d}\tau + k \int_0^{t-T} \frac{g(\tau)}{\sqrt{(t-T)-\tau}} \mathrm{d}\tau. \tag{2.60}$$

The second term in Eq. (2.60) is basically the integral term for the time instant, $(t-T)$ multiplied by the displacement ratio, k. Therefore, Eq (2.60) simplifies to

$$I_B(t) = \int_0^T \frac{g(\tau)}{\sqrt{t-\tau}} \mathrm{d}\tau + kI_B(t-T). \tag{2.61}$$

Substituting $t = mT$ in Eq. (2.61):

$$I_B(mT) = \int_0^T \frac{g(\tau)}{\sqrt{mT-\tau}} \mathrm{d}\tau + kI_B((m-1)T). \tag{2.62}$$

This is a recursive relation which relates the integral term at the mth cycle with the term at the $(m-1)$th cycle. Expanding for all the cycles, we obtain

$$I_B(mT) = \sum_{i=1}^{m} k^{m-i} \int_0^T \frac{g(\tau)}{\sqrt{iT-\tau}} \mathrm{d}\tau. \tag{2.63}$$

We get the following inequality from Eq. (2.63):

$$I_B(mT) > \left(\int_0^T g(\tau)\mathrm{d}\tau\right)\sum_{i=1}^{m}\frac{k^{m-i}}{\sqrt{iT}}, \tag{2.64}$$

which further leads to

$$I_B(mT) > \left(\int_0^T g(\tau)\mathrm{d}\tau\right)\sum_{i=1}^{m}\frac{k^{m-i}}{\sqrt{mT}}. \tag{2.65}$$

Eq. (2.65) sets a lower limit on the integral. For clustering, we know that both the fluid and particle velocities decrease with time, and hence the displacement ratio, $k < 1$. Also, since we are interested in the long term behavior of the particle, the number of cycles, m is much larger than 1. The summation term in the lower bound represents an infinite geometric progression (GP), which can be simplified by the sum of an infinite GP. Hence, Eq. (2.65) gets simplified to

$$I_B(mT) > \frac{1}{\sqrt{mT}}\left(\frac{1}{1-k}\right)\left(\int_0^T g(\tau)\mathrm{d}\tau\right). \tag{2.66}$$

We denote the Basset history term as F_B, where

$$F_B(mT) = \sqrt{\frac{3\beta}{\pi}}\left(I_B(mT) + \frac{u(0)-v(0)}{\sqrt{mT}}\right) \tag{2.67}$$

Using Eqs. (2.66) and (2.67) and noting $t = mT$, we get

$$F_B(t) > \sqrt{\frac{3\beta}{\pi}}\frac{1}{\sqrt{t}}\left(\frac{1}{1-k}\right)\left(\int_0^T g(\tau)\mathrm{d}\tau\right) + \sqrt{\frac{3\beta}{\pi}}\left(\frac{u(0)-v(0)}{\sqrt{t}}\right) \tag{2.68}$$

Eq. (2.68) indicates that the Basset term after m cycles is at least of the order of $\frac{1}{\sqrt{t}}$ or $\frac{1}{\sqrt{mT}}$. The other terms, namely the added mass, drag, and pressure, as well as the particle inertia (on the left hand side) in the Maxey–Riley equation, decrease exponentially with the number of cycles, m and clearly scale with a much smaller value (than $\frac{1}{\sqrt{t}}$). This is not physically possible. Hence, our assumption that the particle displacement varies exponentially for clustering is not true, which is further validated with results obtained by numerical integration as shown in Figure 2.8 (b).

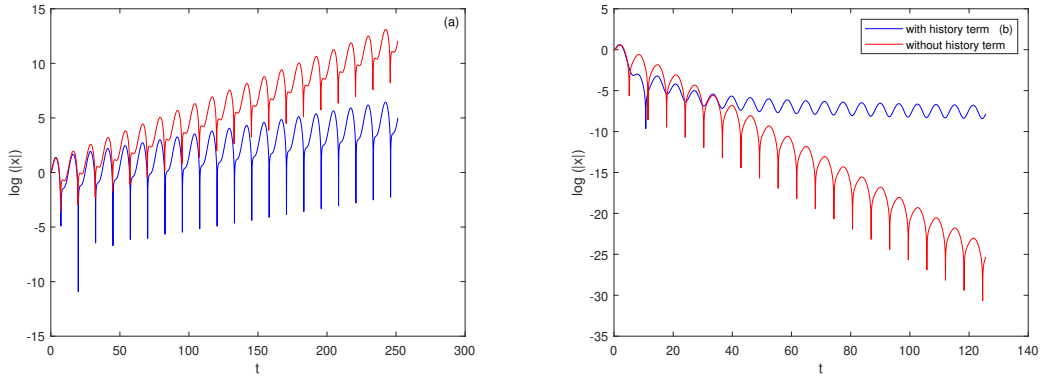

Figure 2.8: The logarithm of the absolute value of particle displacement as a function of time (a) for dispersion, and (b) for clustering, with (in blue), and without (in red) the history term.

For dispersion, $k > 1$. Hence, we can use Eq. (2.65) to get a relation for F_B after m cycles as follows:

$$F_B(mT) > \sqrt{\frac{3\beta}{\pi}}\frac{1}{\sqrt{t}}\left(\frac{k^m-1}{k-1}\right)\left(\int_0^T g(\tau)\mathrm{d}\tau\right) + \sqrt{\frac{3\beta}{\pi}}\left(\frac{u(0)-v(0)}{\sqrt{t}}\right). \tag{2.69}$$

The difference with Eq. (2.68) arises due to whether the displacement ratio, k, is lesser or greater than 1. Since, in this case, $k^m >> 1$, Eq. (2.69) becomes:

$$F_B(mT) > \sqrt{\frac{3\beta}{\pi}}\frac{1}{\sqrt{t}}\left(\frac{k^m}{k-1}\right)\left(\int_0^T g(\tau)\mathrm{d}\tau\right) + \sqrt{\frac{3\beta}{\pi}}\left(\frac{u(0)-v(0)}{\sqrt{t}}\right). \tag{2.70}$$

The term $(u(0) - v(0)) / \sqrt{t}$ scales with $1/\sqrt{t}$ and has a negligible contribution to the dynamics for dispersion. We see that the lower bound has a component k^m which scales exponentially with the number of cycles. Later on, we show numerically, that x varies exponentially with time. Therefore, dispersion can be quantified using the Lyapunov exponent.

We numerically find out how x varies as a function of t from Eq. (2.56) using a time integration scheme as we did before. The Basset term needs special treatment as it is an improper integral. This was the first issue we faced while working on the problem since the ordinary trapezoidal rule cannot be applied. We use an alternate trapezoidal-based (TB) method instead, which was used in

[44] to evaluate the history term. The basic idea of the TB method is that instead of linearly interpolating the whole term inside the integral, we represent the linear interpolant of $g(\tau)$ as $P(\tau)$ and then find the exact integral of $P(\tau)/\sqrt{t-\tau}$. At any time t, we discretize the time domain into N subdomains such that $\Delta t = t/N$ and $\tau_n = t - n\Delta t$ for $n = 0, 1, \ldots, N$. Now, $I_B(t)$ is given by

$$I_B(t) = \int_0^t \frac{g(\tau)}{\sqrt{t-\tau}} \mathrm{d}\tau. \tag{2.71}$$

By linearly interpolating $g(\tau)$ for each time interval, Eq. (2.71) becomes

$$I_B(t) \approx \sum_{n=1}^{N} \int_{\tau_n}^{\tau_{n-1}} \frac{g_n + (g_{n-1} - g_n)(\tau - \tau_n)/\Delta t}{\sqrt{t-\tau}} \mathrm{d}\tau, \tag{2.72}$$

where $g_n = g(\tau_n)$. It can be shown that this integration leads to

$$\begin{aligned} I_B(t) \approx \frac{4}{3} g_0 \sqrt{\Delta t} + g_N \frac{\sqrt{\Delta t}(N - \frac{4}{3})}{(N-1)\sqrt{N-1} + (N - \frac{3}{2})\sqrt{N}} + \sqrt{\Delta t} \\ \times \sum_{n=1}^{N-1} g_n \left(\frac{n + \frac{4}{3}}{(n+1)\sqrt{n+1} + (n + \frac{3}{2})\sqrt{n}} + \frac{n - \frac{4}{3}}{(n-1)\sqrt{n-1} + (n - \frac{3}{2})\sqrt{n}} \right). \end{aligned} \tag{2.73}$$

The value of g should be known at all n instants according to Eq. (2.73). Therefore, we treat it as a vector, $\mathbf{g}$, where at each step after we evaluate $\mathrm{d}v/\mathrm{d}t$ and $\mathrm{d}u/\mathrm{d}t$, we add another element to it corresponding to that time instance. The other force terms, namely added mass, drag, and pressure are evaluated as before. Now, the part with g_0 is treated differently to ensure stability. Since, we know that

$$g_0(t) = \frac{\mathrm{d}}{\mathrm{d}t} u(t) - \frac{\mathrm{d}}{\mathrm{d}t} v(t), \tag{2.74}$$

we bring the $\mathrm{d}v/\mathrm{d}t$ term on the left-hand side and add only the $\mathrm{d}u/\mathrm{d}t$ part to F_B. Therefore, the acceleration of the particle is governed by the form

$$\left(1 + \frac{4}{3}\sqrt{\frac{3\beta}{\pi}}\sqrt{\Delta t}\right) \frac{\mathrm{d}v}{\mathrm{d}t} = \sum F, \tag{2.75}$$

where $\sum F$ is the sum of all the force terms minus the $\mathrm{d}v/\mathrm{d}t$ part. This process is repeated for all time instances.

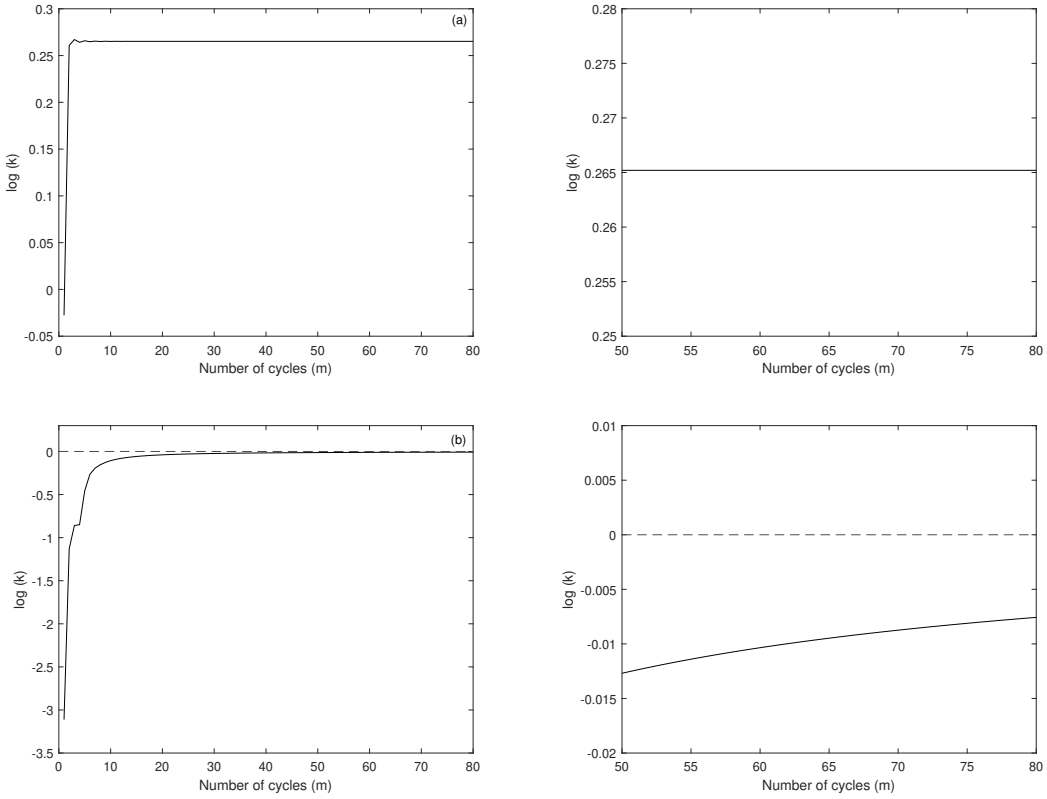

Figure 2.9: The logarithm of the displacement ratio, k as a function of the number of cycles, m for (a) dispersion and (b) clustering. On the right, we have the zoomed in versions of the plots to show a constant value of k for dispersion and an asymptotic value for clustering.

Although, we know how to find $x(t)$, evaluating the Lyapunov exponent for the dispersion case is still a challenge. The method of eigenvalues discussed under Section 2.3.2 cannot be applied because of the history term. Hence, we use the brute-force approach of finding out $x(t)$ for multiple cycles, and then finding out the exponent corresponding to the last cycle. We have to keep in mind however that the difference between the exponents of the last and penultimate cycle should be small enough to ensure that they have converged to the Lyapunov exponent. For example, in Figure 2.10 (a) we find out x for 10 cycles for each ϕ and β. The maximum normalized difference that we get for real (λ) for the 10th and 9th cycle in that case is 7.59×10^{-3} which is small enough to consider

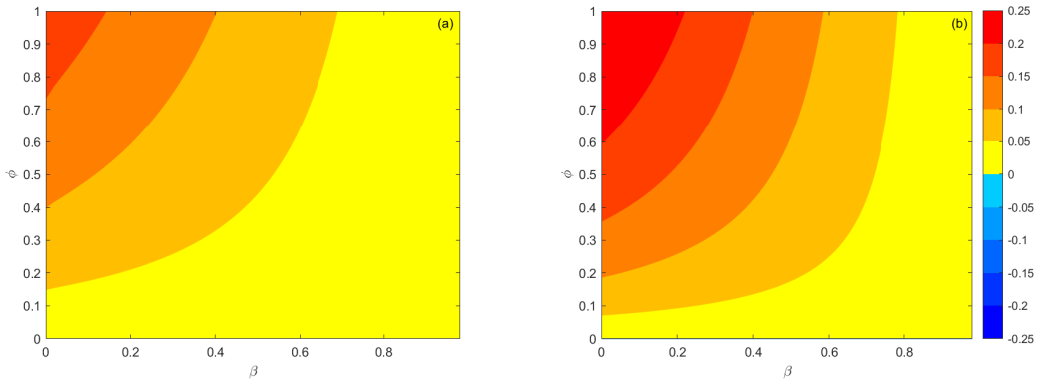

Figure 2.10: The rate of expansion, real (λ) as a function of β and ϕ (a) with the history term and (b) without the history term for $0 \leq \beta < 1$, $\phi > 0$ and $\omega = 0.1$ where only dispersion is observed.

convergence.

Figure 2.8 (a) shows how the logarithm of the absolute value of particle displacement varies with time for $\sqrt{-2\phi} = 1$, $\omega = 0.5$ and $\beta = 0.1$. For dispersion as we mentioned, the particle displacement is an exponential function of time like the case without the Basset term. Hence we can define a Lyapunov exponent in the dispersion regime. For example in this case, we get a constant value of $\log(k) = 0.265$ as it is evident in Figure 2.9 (a) and the Lyapunov exponent is $0.265/(2\pi/0.5) \approx 0.02$.

For clustering however, the displacement does not vary exponentially with time unlike the case when the history term was neglected. Figure 2.8 (b) shows the contrast between the scenarios when we neglect the Basset history Force (in red) and when the term is included (in blue). The displacement ratio, k in this case is not constant and $\log(k)$ asymptotically reaches the value of 0 as it is evident from Figure 2.9 (b). This means that as the time increases, the tendency of the particles to mimic the background flow increases.

Next, we want to see how the introduction of the history term changes the

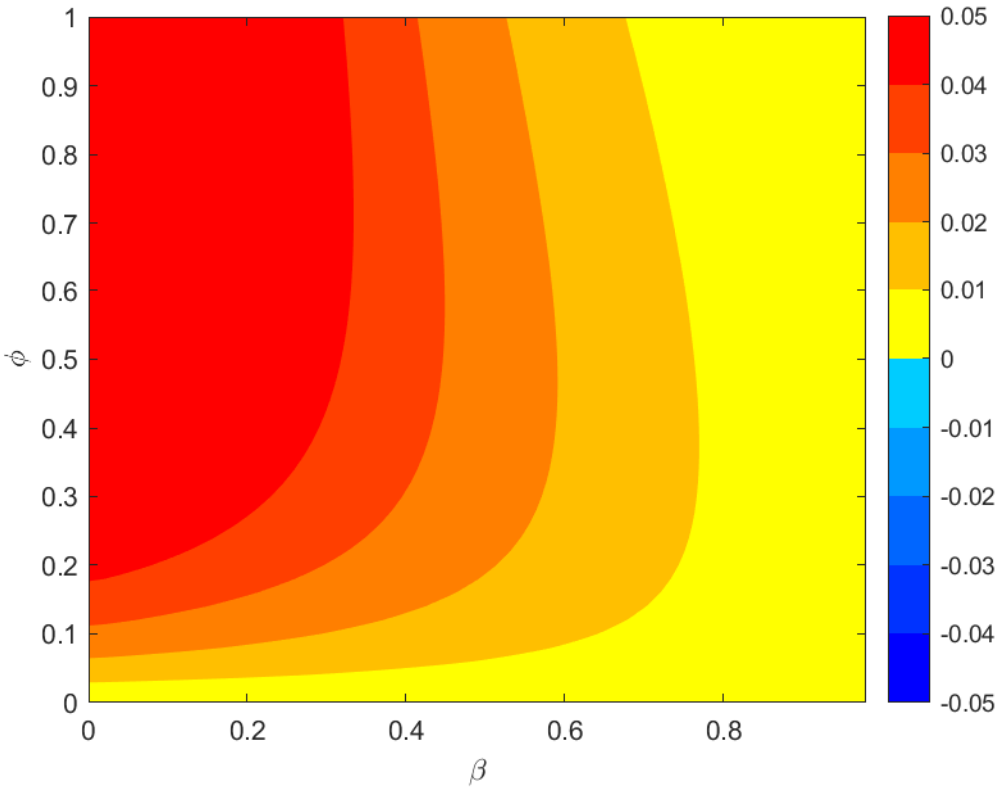

Figure 2.11: The value obtained after subtracting real (λ) with the history term from real (λ) without the history term for $0 \leq \beta < 1$, $\phi > 0$ and $\omega = 0.1$.

value of the Lyapunov exponent for dispersion. Hence, we shift our focus to a region where only dispersion is observed. Particles heavier than the fluid in a rotating flow satisfy this condition as shown in Figure 2.10 (b). Figure 2.10 (a) shows that in spite of the inclusion of the history term, the particles still undergo dispersion. However, the interesting thing that we observe in Figure 2.11 is that the rate of dispersion is always higher for the case without the history term. In other words, the inclusion of the history term lowers the Lyapunov exponent when particles are dispersing.

The important question that is yet to be addressed is how can we quantify the clustering phenomenon. Since the log ($|x|$) vs t plot didn't show an exponential variation with t, we had to analytically validate that exponential variation is

not possible for clustering. One way of addressing that issue is to approximate x using another function type and then use the characteristics of that function type to quantify clustering. This is the scope for future research.

To summarize, we start with the inclusion of the history term in the Maxey–Riley equation. We validate the fact that for clustering, displacement is not an exponential function of time unlike the case with no history term which is consistent with our observations. We also find out that for dispersion, the variation is still exponential and hence can be quantified by the Lyapunov exponent. Next, we compare the Lyapunov exponents for the cases with and without the history term. We choose a regime where we only observe dispersion. One such example would be particles heavier than the fluid in a rotating flow (or $0 \leq \beta < 1$ and $\phi > 0$). We see that these particle still undergo dispersion but there is always a decrease in the Lyapunov exponent.

2.4 Conclusion

We have derived an analytical expression (2.41) for the Lyapunov exponent as a function of the Stokes number and the particle-to-fluid density ratio. The Lyapunov exponent is the same in each direction, hence analyzing one direction would suffice. Since the densities of the particle and the fluid are comparable, the added mass and the pressure forces affect the particle dynamics. We employ a one-dimensional unimodal canonical flow that has been shown to show a very good agreement with the analytical results, albeit at infinite density ratio which we have referred to as IDR, to validate our results. Hence our analysis is more general, and at the limits of infinite density ratio, it converges to the result

derived in IDR. Further, our analysis explains the non-monotonic trend of clustering for finite particle-to-fluid density ratios, which RM failed to predict. We predict that in the straining regime, we might observe clustering or dispersion depending on the Stokes number. An increase in the particle-to-fluid density ratio leads to an increase in clustering and a decrease in dispersion. Similarly, in the rotating regime, we predict no clustering, and an increase in dispersion for higher values of density ratio. We also show that there exists a lower bound on particle clustering corresponding to real(λ) = -0.5. We also observed that there exists a condition for which there can be dispersion for neutrally buoyant particles, which is further validated by our numerical results. Finally, we study how the inclusion of the Basset history term affects our analysis. For clustering, we show that the separation distance between a pair of particles will no longer be exponential in time whereas dispersion can still be quantified by the Lyapunov exponent, which decreases when the history term is considered.

CHAPTER 3

SPECTRAL STOKES SOLVER FOR TIME-PERIODIC FLOWS

3.1 Introduction

In this chapter, we first introduce our algorithm, which we call the complex-valued Stokes Solver (SCVS). It is based on finite element modeling in the spectral domain. The result of the modeling is a complex-valued linear system which we solve using GMRES.

Next, we compare the performance of SCVS against RBVMS for an oscillating flow in 3D pipe for different flow conditions. For validation, we also compare our results to an analytical prediction that exists for such flows. We finally compare the performance of SCVS to a more similar solver called MSS before concluding at the end.

3.2 SCVS

We consider low Reynolds number flow in a domain Ω with boundary $\Gamma = \partial\Omega$ that is governed by the unsteady Stokes equations given by

$$\begin{aligned} \rho\frac{\partial u}{\partial t} &= -\nabla p + \nabla\cdot(\mu\nabla u) \quad \text{in } \Omega, \\ \nabla\cdot u &= 0 \quad \text{in } \Omega, \\ u &= g \quad \text{on } \Gamma_{\mathrm{g}}, \\ (-pI + \mu\nabla u)\cdot n &= h \quad \text{on } \Gamma_{\mathrm{h}}, \end{aligned} \tag{3.1}$$

where $u(x,t)$ refers to the velocity of the fluid at location x and time t, $p(x,t)$ is the pressure, ρ is the density, Γ is the boundary, n is the outward normal vector, and μ is the dynamic viscosity. g and h refer to the imposed velocity and traction on the Dirichlet Γ_{g} and Neumann Γ_{h} boundaries, respectively, where $\Gamma = \Gamma_{\mathrm{g}} \cup \Gamma_{\mathrm{h}}$. Additionally, the boundary conditions are assumed to be periodic with a time period of T.

To represent Eq. (3.1) in the spectral domain, we make use of Fourier transformation. Hence, the velocity and pressure can be written as,

$$\begin{aligned} u(x,t) &= \sum_i \tilde{u}_i(x) e^{\hat{j}\omega_i t}, \\ p(x,t) &= \sum_i \tilde{p}_i(x) e^{\hat{j}\omega_i t}, \end{aligned} \tag{3.2}$$

where $\hat{j} = \sqrt{-1}$. Here the frequency ω_i is defined in terms of the period T as $\omega_i = 2\pi i/T$ for $i = 0, 1, \ldots, N_{\mathrm{m}}$, N_{m} being the largest mode. For cardiovascular flows, T is the cardiac cycle, which is the time period of the boundary conditions. We can represent the Dirichlet and Neumann boundary conditions in the spectral domain as

$$\begin{aligned} g(x,t) &= \sum_i \tilde{g}_i(x) e^{\hat{j}\omega_i t} \\ h(x,t) &= \sum_i \tilde{h}_i(x) e^{\hat{j}\omega_i t} \end{aligned} \tag{3.3}$$

Eq. (3.1) thus becomes,

$$\begin{aligned} \hat{j}\omega_i \rho \tilde{u}_i &= -\nabla \tilde{p}_i + \nabla \cdot (\mu \nabla \tilde{u}_i) \quad \text{in } \Omega, \\ \nabla \cdot \tilde{u}_i &= 0 \quad \text{in } \Omega, \\ \tilde{u}_i &= \tilde{g}_i \quad \text{on } \Gamma_{\mathrm{g}}, \\ (-\tilde{p}_i I + \mu \nabla \tilde{u}_i) \cdot n &= \tilde{h}_i \quad \text{on } \Gamma_{\mathrm{h}}. \end{aligned} \tag{3.4}$$

The term on the left hand side is complex unless $\omega_i = 0$. The constraint $\omega_i = 0$

corresponds to the steady state. Since these equations are independent boundary value problems, we drop the subscript i, in our analysis.

Next, we define the weak form of Eq. (3.4). The weak form of Eq. (3.4) is stated as follows. For a given frequency ω, find $\tilde{u} \in \mathcal{S}$ and $\tilde{p} \in \mathcal{P}$ such that for any $w \in \mathcal{W}$ and $q \in \mathcal{Q}$

$$\begin{aligned} B_{\mathrm{G}}(w, q; \tilde{u}, \tilde{p}) &= F_{\mathrm{G}}(w, q), \\ B_{\mathrm{G}} &= \int_{\Omega} \left[\hat{j}\omega\rho w \cdot \tilde{u} + \nabla w : (-\tilde{p}I + \mu\nabla\tilde{u}) + q\nabla \cdot \tilde{u} \right] \mathrm{d}\Omega, \\ F_{\mathrm{G}} &= \int_{\Gamma_{\mathrm{h}}} w \cdot \tilde{h} \mathrm{d}\Gamma, \end{aligned} \tag{3.5}$$

holds. In Eq. (3.5), w and q are test functions for velocity and pressure, respectively, and

$$\begin{aligned} \mathcal{S} &= \left\{ \tilde{u} | \tilde{u}(x) \in (H^1)^{n_{\mathrm{sd}}},\ \tilde{u} = \tilde{g} \text{ on } \Gamma_{\mathrm{g}} \right\}, \\ \mathcal{W} &= \left\{ w | w(x) \in (H^1)^{n_{\mathrm{sd}}},\ w = 0 \text{ on } \Gamma_{\mathrm{g}} \right\}, \\ \mathcal{P} &= \left\{ \tilde{p} | \tilde{p}(x) \in L^2 \right\}, \\ \mathcal{Q} &= \left\{ q | q(x) \in L^2 \right\}, \end{aligned} \tag{3.6}$$

where $\mathcal{S}$ and $\mathcal{P}$ are the velocity and pressure solution, respectively. $\mathcal{W}$ and $\mathcal{Q}$ are the test function spaces. L^2 denotes the space of scalar-valued functions that are square-integrable on Ω, $(H^1)^{n_{sd}}$ denotes the space of vector-valued functions with square-integrable derivatives on Ω, and n_{sd} is the number of spatial dimensions.

We denote the finite-dimensional subspace of $\mathcal{S}$, $\mathcal{W}$, $\mathcal{P}$, and $\mathcal{Q}$ by $\mathcal{S}^h$, $\mathcal{W}^h$, $\mathcal{P}^h$, and $\mathcal{Q}^h$, respectively. Then, we represent the discrete form of Eq. (3.5) using Galerkin's approximation. Namely, we seek $\tilde{u}^h \in \mathcal{S}^h$ and $\tilde{p}^h \in \mathcal{P}^h$ such that for any $\tilde{w}^h \in \mathcal{W}^h$ and $\tilde{q}^h \in \mathcal{Q}^h$

$$B_{\mathrm{G}}\left(w^h, q^h; \tilde{u}^h, \tilde{p}^h\right) = F_{\mathrm{G}}\left(w^h, q^h\right), \tag{3.7}$$

holds. In writing Eq. (3.7), we assumed $\Omega^h = \Omega$, i.e., the computational domain after discretization remains unchanged. If the two are different, all the integrals are done over Ω^h instead when computing B_{G} and F_{G} in Eq. (3.7).

The Galerkin's formulation has a saddle-point nature, which leads to a singular system if the same shape functions for velocity and pressure are used. Many techniques have been developed in the past to overcome this issue, like penalty techniques [45], mixed-element [46] and stabilized finite element methods [47]. In the present study, we use the mixed finite element method. Basically, we use linear and quadratic shape functions for pressure and velocity, respectively, to satisfy inf-sup condition (also known as LBB condition) [48, 49, 50]. In 3D, we use linear tetrahedral elements with 4 nodal points for pressure and quadratic shape functions with 10 nodes for velocity. We denote the corresponding linear and quadratic shape functions at global node A by $N_A(x)$ and $M_A(x)$ respectively. Therefore, velocity and pressure and their corresponding test functions in terms of the aforementioned shape functions can be represented as

$$
\begin{aligned}
w^h(x) &= \sum_{A \in \eta \setminus \eta_{\mathrm{g}}} M_A(x) W_A, \\
q^h(x) &= \sum_{A \in \hat{\eta}} N_A(x) Q_A, \\
\tilde{u}^h(x) &= \sum_{A \in \eta \setminus \eta_{\mathrm{g}}} M_A(x) U_A + \sum_{A \in \eta_{\mathrm{g}}} M_A(x) G_A, \\
\tilde{p}^h(x) &= \sum_{A \in \hat{\eta}} N_A(x) P_A,
\end{aligned}
\tag{3.8}
$$

where η, η_{g}, and $\hat{\eta}$ are the velocity nodes, velocity nodes on the Dirichlet boundaries, and pressure nodes, respectively. U_A, P_A, W_A, Q_A in Eq. (3.8) are the velocity and pressure unknowns and their respective test functions. G_A is the prescribed velocity defined on the Dirichlet boundaries after discretization such

that

$$\tilde{g}^h(x) = \Pi^h \tilde{g}(x) = \sum_{A \in \eta_g} M_A(x) G_A, \tag{3.9}$$

where $\Pi^h \tilde{g}$ is an operator that projects $\tilde{g}$ to the finite-dimensional discrete space. Substituting Eq. (3.8) in Eq. (3.7) we get the following linear system

$$AX = R, \tag{3.10}$$

where

$$A = \begin{bmatrix} K & D \\ D^{\mathrm{T}} & 0 \end{bmatrix}, \quad X = \begin{bmatrix} U \\ P \end{bmatrix}, \quad R = \begin{bmatrix} B \\ 0 \end{bmatrix}. \tag{3.11}$$

Here, K and D are block matrices and B is a vector which are given by,

$$\begin{aligned} K_{AB} &= \int_\Omega \left(\hat{j}\omega\rho M_A M_B + \mu \nabla M_A \cdot \nabla M_B \right) I \mathrm{d}\Omega, \\ D_{AB} &= -\int_\Omega \nabla M_A N_B \mathrm{d}\Omega, \\ B_A &= \int_{\Gamma_h} M_A \tilde{h} \mathrm{d}\Gamma - \mathrm{K_{AB}} \mathrm{G_B}. \end{aligned} \tag{3.12}$$

The solution to this is obtained using the Generalized minimal residual method (GMRES) method [51] with a Jacobi preconditioner.

3.3 Results

In this section, we will establish the relative accuracy and cost of the SCVS algorithm against a standard RBVMS solver and an in-house MSS solver. The details pertaining to the RBVMS algorithm are included in Appendix A. We have considered creeping flow through a 3D pipe as our test case for comparison. The analytical solution for this problem is available and it will be employed to further validate the results. The geometry has been discretized using tetrahedral elements. We have used Tetgen [52] and Simvascular [53] software for

mesh generation and an-house script for node insertion. We first compare our results with a standard RBVMS solver. Since SCVS uses mixed QM mesh unlike RBVMS, which uses linear mesh for discretization, for a more thorough comparison, we also compare SCVS to an in-house solver called MSS, which uses QM mesh as well. The only difference is that MSS, like RBVMS, solves the Stokes equation in the time domain unlike SCVS, which solves it in the spectral domain.

3.3.1 Comparison with RBVMS

Since the SCVS and RBVMS simulations are performed using quadratic and linear shape functions, comparison is done betweeen those pairs of meshes which have similar degrees of freedom. A total of five cycles or 10,000 time steps are simulated to achieve cycle-to-cycle convergence for the RBVMS solver. All the results correspond to the last simulated cycle to get rid of the transient part of the solution. For all cases, the Reynolds number is kept very small ($\mathrm{Re} < 10^{-3}$) to neglect the effect of inertia or non-linearity. The Reynolds number depends on the maximum flow rate through the boundaries, the diameter of the pipe, and the kinematic viscosity, $\nu = \mu/\rho$.

Table 3.1: Meshes used for discretization shown in Figure 3.1. QM and LM refer to mixed quadratic-linear and linear tetrahedral meshes, which are employed in the SCVS and the RBVMS simulations, respectively. N_{ele}, N_{nds}, and N_{dof} denote the numbers of elements, nodes, and degrees of freedom, respectively.

Mesh	SCVS				RBVMS			
	QM1	QM2	QM3	QM4	LM1	LM2	LM3	LM4
N_{ele}	24,450	49,388	95,524	162,444	207,063	374,852	728,922	1,197,044
N_{nds}	37,469	70,872	133,645	225,610	37,401	64,434	122,291	197,660
N_{dof}	113,193	221,894	418,400	705,311	149,604	257,736	489,164	790,640

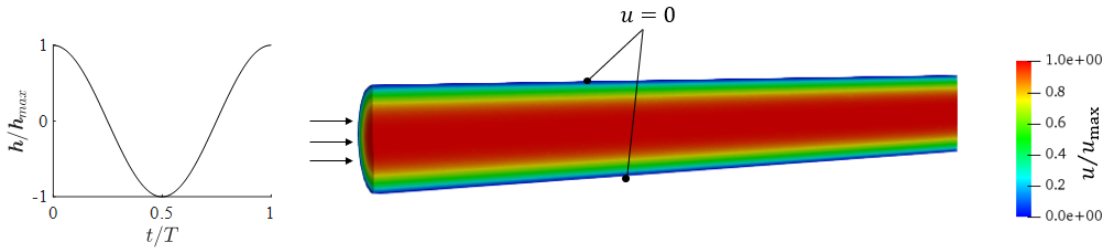

Figure 3.1: Schematic of oscillatory creeping flow in a pipe. $h(t)/h_{\max}$ refers to the imposed Neumann boundary condition at the inlet as a function of time. The contour of normalized radial velocity magnitude is shown for $W = 8\pi$ case at $t = T/4$ obtained from the SCVS solver.

As mentioned before, we use GMRES to solve the linear system for both SCVS and RBVMS with $\epsilon_{\mathrm{L}} = 10^{-6}$ as the tolerance. Both the RBVMS and the SCVS solvers are based on an in-house finite element solver [54, 55, 56], which is written in object-oriented Fortran and parallelized using the MPI library. However since the equations for SCVS have complex valued terms, we need to make changes to the GMRES solver accordingly.

Coming back to the test case, we have considered a pipe with an aspect ratio of $L/R = 15$ with a cosinusoidal inlet (on the left) and zero outlet Neumann boundary condition (Figure 3.1). These boundary conditions produce a solution that corresponds to the fully developed condition observed in an infinitely long pipe. Our analysis is limited to three Womersley numbers $W = \omega R^2/\nu = 8\pi, 40\pi$ and 80π, with R denoting the radius of the pipe. For each of RBVMS and SCVS, simulations are performed in four different meshes (Table 3.1). The number of elements in corresponding meshes is selected such that the number of nodes is roughly the same for both solvers. Overall, the element size normalized by the pipe radius varies from 0.0340 to 0.228 among simulated cases.

For an oscillatory flow in a pipe, the solution in the spectral domain is expressed as [57]

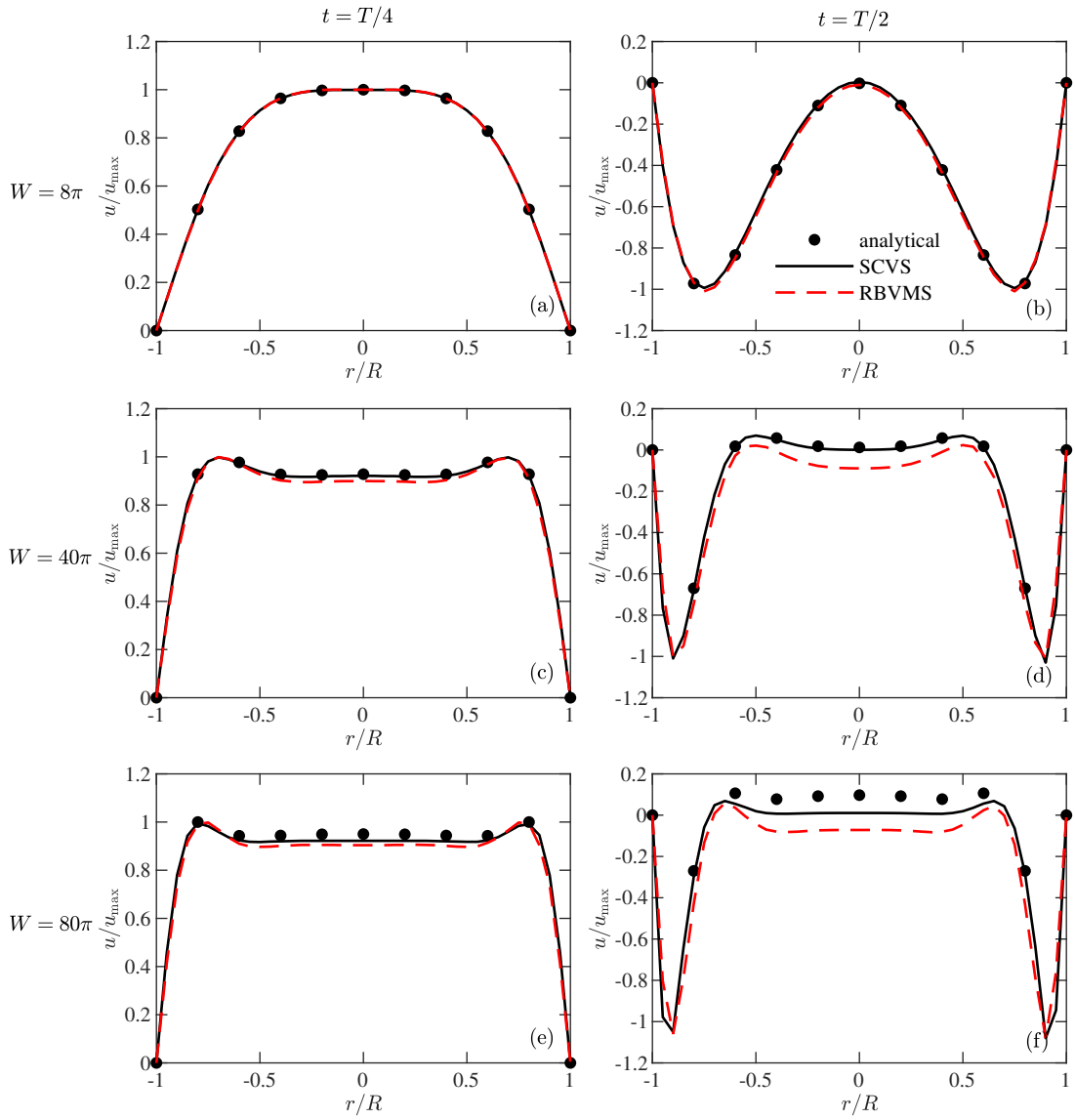

Figure 3.2: Normalized velocity profiles as a function of the normalized radial distance for an oscillatory creeping pipe flow (shown in Figure 3.1) predicted using the SCVS (solid black), the RBVMS (dashed red), and analytical solution (circles). The results on the left and right columns are at $t = T/4$ and $t = T/2$, respectively, and those on the first, second, and third row correspond to $W = 8\pi$, 40π, and 80π, respectively. Computations are performed on QM4 and LM4 grids for the SCVS and the RBVMS, respectively. All the results are normalized using the maximum velocity from the analytical solution $u_{\max}$.

$$\tilde{u}_x(r,\omega) = \begin{cases} \dfrac{\tilde{h}_x}{4\mu L}(R^2 - r^2), & \omega = 0, \\ \\ -\dfrac{\hat{j}\tilde{h}_x}{\rho L \omega}\left[1 - J_0(\Lambda)^{-1} J_0(\Lambda \dfrac{r}{R})\right], & \omega \neq 0, \end{cases} \tag{3.13}$$

where $\Lambda^2 = -\hat{j}W$ and J_0 is the zero order Bessel function of the first kind. This solution can be expressed in time using

$$u_x(r,t) = \text{real}\left\{\tilde{u}_x(r,\omega)e^{\hat{j}\omega t}\right\}. \tag{3.14}$$

Figure 3.2 illustrates $u_x(r, T/4)$ and $u_x(r, T/2)$ obtained using the SCVS solver, the RBVMS solver and the analytical formula in Eq. (3.14) at $W = 8\pi$, 40π, and 80π. These results correspond to the finest grids, namely QM4 and LM4 in Table 3.1. The greater accuracy of SCVS stems from the use of Quadratic shape functions as compared to the use of linear shape functions for RBVMS. To study mesh convergence, we define the total error, e as

$$e(t) = \frac{||u(x,t) - u^h(x,t)||_{L_2(\Omega)}}{||u(x,t)||_{L_2(\Omega)}}. \tag{3.15}$$

The overall error is basically the difference between the calculated velocity $u^h(x,t)$ and the reference velocity $u(x,t)$ normalized by the reference velocity over the entire domain and the $L_2(\Omega)$ norm is defined as $||u||^2_{L_2(\Omega)} = \int_\Omega u \cdot u \mathrm{d}\Omega$. Overall, we see a very good match between the analytical predictions and the results obtained using SCVS.

Figure 3.3 shows how the error at $t = T/2$, $e(T/2)$ varies with CPU hours at Womersley numbers, W = 8π (black), W = 40π (red) and W = 80π (blue). This is of particular use when we want to see the cost we will incur and the mesh we want to use for both SCVS and RBVMS for a given flow condition if we want to achieve a predefined accuracy. For example, the coarsest grid for SCVS has

a similar accuracy (slightly better) to the finest grid for RBVMS but there is a reduction of cost by three orders of magnitude for $W = 80\pi$.

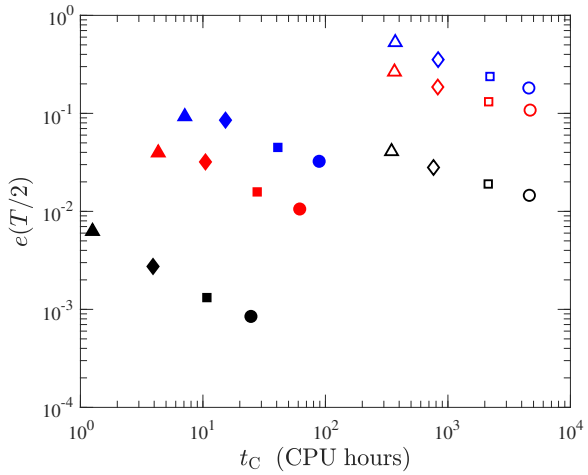

Figure 3.3: Relative error $e(T/2)$ as a function of the computational cost t_C. Symbols with the same color should be compared. The solid symbols correspond to the SCVS and hollow to the RBVMS. The circle, square, diamond, and triangle symbols correspond to QM4/LM4, QM3/LM3, QM2/LM2, and QM1/LM1 meshes listed in Table 3.1. The black, red, and blue colors correspond to $W = 8\pi$, 40π, and 80π, respectively. These results show that the SCVS, compared to the RBVMS, always provides a higher accuracy at a lower cost.

3.3.2 Comparison with MSS

For an apple-to-apple comparison with SCVS, we have solved the unsteady Stokes equations in time. We call this solver MSS and it is identical to the SCVS solver, except for the domain in which the equations are solved. The weak form of the MSS states: find $u \in \mathcal{S}$ and $p \in \mathcal{P}$, such that for all $w \in \mathcal{W}$ and $q \in \mathcal{Q}$

$$B_G(w, q; u, p) = F(w, q), \tag{3.16}$$

where

$$\begin{aligned} B_G &= \int_\Omega \left[\rho w \cdot \dot{u} + \nabla w : (-pI + \mu \nabla^s u) + q \nabla \cdot u\right] d\Omega, \\ F &= \int_{\Gamma_h} w \cdot h d\Gamma. \end{aligned} \tag{3.17}$$

Eq. (3.17) is discretized using tetrahedral elements that were used for the SCVS. To relate $\dot{u}$ to u and integrate the resulting equations in time, the second order implicit generalized-α method is adopted [58]. The spectral radius of the infinite time step, which appears in the generalized-α time integration scheme, is set to 0.2 which is seen to have no influence on the results in this study. The working of the generalized-α time-integration scheme is explained in greater detail below.

First, we start with zero initial conditions everywhere. At each time step, we predict unknowns at the next time step as $\dot{u}_{n+1} = \frac{\gamma-1}{\gamma}\dot{u}_n$, $u_{n+1} = u_n$, and $p_{n+1} = p_n$. Next, the unknowns are computed at an intermediate time, namely $\dot{u}_{n+\alpha_m}$, $u_{n+\alpha_f}$ and $p_{n+\alpha_f}$ as

$$\begin{aligned} \dot{u}_{n+\alpha_m} &= \dot{u}_n + \alpha_m(\dot{u}_{n+1} - \dot{u}_n), \\ u_{n+\alpha_f} &= u_n + \alpha_f(u_{n+1} - u_n), \\ p_{n+\alpha_f} &= p_n + \alpha_f(p_{n+1} - p_n), \end{aligned} \tag{3.18}$$

where $\alpha_f = (1+\rho_\infty)^{-1}$, $\alpha_m = (3-\rho_\infty)(2+2\rho_\infty)^{-1}$, and $\gamma = 0.5+\alpha_m-\alpha_f$ are parameters that depend on the spectral radius of infinite time step ρ_∞ (0.2 in our case). These values are then employed to calculate B_G in Eq. (3.17). After discretization and Newton-Raphson linearization, we get the following linear system

$$\begin{bmatrix} K & G \\ D & 0 \end{bmatrix} \begin{bmatrix} \Delta\dot{u} \\ \Delta p \end{bmatrix} = - \begin{bmatrix} R_M \\ R_C \end{bmatrix}, \tag{3.19}$$

where

$$\begin{aligned} K &= \frac{\partial R_M}{\partial \Delta\dot{u}}, \\ G &= \frac{\partial R_M}{\partial \Delta p}, \\ D &= \frac{\partial R_C}{\partial \Delta\dot{u}}. \end{aligned} \tag{3.20}$$

R_M and R_C are the momentum and continuity residuals and can be evaluated by substituting Eq. (3.8) in Eq. (3.17). $\Delta\dot{u}$ and Δp are correction to our initial

prediction of unknowns at the next time step. Unlike the RBVMS, the MSS does not have stabilization terms, hence there is a zero block in the matrix in Eq. (3.19) The continuity equation does not depend on the pressure. The linear system in Eq. (3.19) is solved iteratively using the GMRES technique. Then the corrections are applied as follows:

$$\begin{aligned} \dot{u}_{n+1} &\leftarrow \dot{u}_{n+1} + \Delta\dot{u}, \\ u_{n+1} &\leftarrow u_{n+1} + \gamma\Delta t\Delta\dot{u}, \\ p_{n+1} &\leftarrow p_{n+1} + \Delta p. \end{aligned} \tag{3.21}$$

Following these corrections, the Newton-Raphson iteration loop will be terminated if the norm of the residual is smaller than a specified tolerance. Otherwise, new intermediate variables are computed via Eq. (3.18) and a new iteration is performed. As mentioned before, for the linear Stokes equation, only one iteration is enough. This entire process is repeated at each time step.

The MSS needs two nested loops: an outer loop for time-stepping, and an inner loop for the linear solver.

Table 3.2: Comparison of the different solvers for the 3D pipe flow at $W = 8\pi$ in terms of computational cost and overall error. QM1 and LM1 meshes from Table 3.1 were used for these computations, with the former being used for the SCVS and MSS and the latter for the RBVMS.

	SCVS	MSS	RBVMS
Mesh	QM1	QM1	LM1
The total computational cost (in CPU hours)	1.25	1522	347
The overall error; $e(T/2)$	6.3×10^{-3}	1.79×10^{-2}	4.1×10^{-2}

In Table 3.2 we compare the overall error, Eq. (3.15) and the cost of MSS with the SCVS and RBVMS solvers for $W = 8\pi$ and $t = T/2$. The details of the meshes used for these computations are reported in Table 3.1, where we use QM1 for the SCVS and MSS and LM1 for the RBVMS.

The huge cost reduction from the MSS to SCVS can be explained by the fact that the SCVS solver performs just one linear solve, whereas the MSS solver performs 10,000 linear solves (each time step requiring one linear solve). However, the performance gap between the MSS and SCVS is 1522/1.25 = 1,220 that is less than 10,000 as the average number of GMRES iterations for the MSS is less than that of the SCVS (i.e., 2,336.7 versus 7,943). Having pure real operations as opposed to complex operations for SCVS in the GMRES solver decreases the performance gap.

To explain the lower performance of the MSS in comparison to the RBVMS, we must analyze the structure of the linear system for these two solvers. Since the MSS does not have stablization terms added unlike the RBVMS (see Appendix A), the discrete form of the continuity equation will not depend on the pressure. This lack of dependence is in contrast to the RBVMS that through $u_{\mathrm{p}} \cdot \nabla q$ term in Eq. (A.2) produces a non-zero block in the tangent matrix in Eq. (3.20). This non-zero block reduces the condition number of the tangent matrix, leading to a much faster convergence rate of the GMRES algorithm for the RBVMS (493.97 for the RBVMS versus 2,336.7 for the MSS).

In terms of error, the SCVS that does not suffer from the time integration error and employs quadratic shape functions for velocity is the most accurate formulation. The SCVS is followed by the MSS solution that contains time integration error and the RBVMS that on top of that error uses linear elements.

The RBMVS is a more widely adopted formulation than the MSS, thus using it as a benchmark can provide a better point of reference. Firstly, as confirmed by the results shown in Table 3.2, in general, the RBVMS performs better than the MSS. Secondly, the cost and convergence properties of the MSS significantly

suffer for larger meshes, making the simulation of some of the cases reported in Section 3.3 nearly impractical.

3.4 Conclusion

In this chapter, we proposed an alternative method for solving time-periodic flows at low Reynolds number. First we transformed the unsteady Stokes equation in the time domain into multiple steady state Stokes equations with a complex source term in the spectral domain. For the class of flows we are interested in, namely cardiovascular flows, we need to solve only a few boundary value problems, each corresponding to one mode. In this way, we get rid of the problems associated with time integration schemes. Next, we derived the weak form of the resultant equations followed by the discrete formulation. Discretization was carried out using mixed quadratic-linear shape functions. We finally obtained a linear system out of each boundary value problem. The linear system is solved using GMRES which had to be modified to accommodate for the complex-valued source term.

To check the performance of SCVS, we compare it against a standard RBVMS solver first for time-periodic flows in a 3D pipe. We see an order of magnitude improvement for accuracy for SCVS compared to RBVMS. We also see two orders of magnitude improvement in CPU hours in comparison to the RBVMS. For a more direct one-one comparison, we compared SCVS against MSS which uses same shape functions as SCVS. We see three orders of magnitude difference in the cost and a better accuracy as well for the SCVS solver. Further improvement in performance through the use of stabilized or penalty formulation as

well as the extension to higher Reynolds numbers remain to be explored in the future.

CHAPTER 4

PRELIMINARY DISCUSSION ON AN INHERENTLY PARALLEL GMRES

The final chapter introduces a very basic discussion on solving a linear system on multiple processors where we want to see whether there is a way of making use of communications and operations (like matrix-vector products and dot products) across the shared nodes to converge to the solution faster. The eventual plan would be to extend this discussion to exascale computing, which is beyond the scope of this thesis. Our discussion will be limited to Krylov subspace methods, particularly GMRES [51]. We take the simple example of a non-dimensional 1D-heat conduction equation to demonstrate our proposed method. The governing differential equation is given by

$$\begin{aligned} \frac{d^2\phi}{dx^2} + f &= 0, \\ \frac{d\phi}{dx}(0) &= -q, \\ \phi(1) &= g. \end{aligned} \tag{4.1}$$

Eq. (4.1) is basically the non-dimensional Poisson Equation in 1D. ϕ is the non-dimensional temperature and $x \in [0,1]$. We have a Neumann Boundary condition on the left side and a Dirichlet Boundary condition on the right side as shown in Figure 4.1. Performing an analysis similar to what we have done in

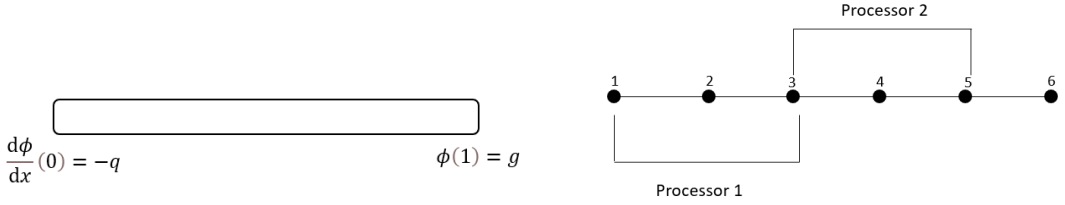

Figure 4.1: Schematic of a rod with an isothermal boundary on the right and a constant heat flux boundary on the left. The rod is discretized uniformly. Nodes 1,2 and 3 and Nodes 3,4 and 5 belong to processors 1 and 2 respectively. Node 3 is shared between both the processors.

Section 3.2, we get a linear system of the form, $\mathcal{A}\boldsymbol{x} = \mathscr{b}$. For demonstration, we have divided the entire domain uniformly into 5 points (with unknown values of ϕ) marked as $1, \ldots, 5$ as shown in Figure 4.1. Point 6 is on the Dirichlet boundary and hence the value is already known. In this linear system, $\boldsymbol{x}$ is the solution vector which needs to be evaluated and can be written as $\boldsymbol{x} = \{\phi_1, \ldots, \phi_5\}^T$, where ϕ_i is the unknown temperature at node i. Our test case involves solving this simple linear system using two processors. The domain is divided into two partitions with nodes 1, 2 and 3 belonging to Processor 1 and nodes 3, 4 and 5 belonging to Processor 2. Therefore, node 3 in our problem is the shared node where communications will take place and which we plan to exploit.

The GMRES method is a Krylov subspace method, which means the unknown vector can be represented as a superposition of several solution candidates which belong to an affine space, known as the Krylov subspace. For a given linear system, $\mathcal{A}x = \mathscr{b}$, $v = \{\mathscr{b}, \mathcal{A}\mathscr{b}, \mathcal{A}^2\mathscr{b}, \mathcal{A}^3\mathscr{b}, \ldots\}$ is the Krylov subspace. The GMRES method approximates the solution vector, $\boldsymbol{x}$ as

$$\boldsymbol{x} \approx \sum_{i=1}^{n} c_i \boldsymbol{v}_i, \tag{4.2}$$

where $\boldsymbol{v}_i$ are vectors of the Krylov subspace, m is the number of vectors, and c_i are variables that are optimized to get the smallest value of the norm of the residual $\mathcal{A}\boldsymbol{x} - \mathscr{b}$.

For each processor there is a local $\boldsymbol{A}$ and a local $\boldsymbol{b}$ obtained by discretization, which we will denote by $\boldsymbol{A}^1$ and $\boldsymbol{b}^1$ for processor 1, and $\boldsymbol{A}^2$ and $\boldsymbol{b}^2$ for processor 2, where $\boldsymbol{A}^1$ and $\boldsymbol{b}^1$ are given by

$$\boldsymbol{A}^1 = \begin{bmatrix} \boldsymbol{A}^1_{11} & \boldsymbol{A}^1_{12} \\ \boldsymbol{A}^1_{21} & A^1_{22} \end{bmatrix}, \quad b^1 = \begin{bmatrix} \boldsymbol{b}^1_1 \\ b^1_2 \end{bmatrix}. \tag{4.3}$$

The superscript 1 indicates that the values are local to processor 1. To make a

one-to-one correspondence to the global numbering depicted in Figure 4.1, the blocks of $\boldsymbol{A}^1$ are

$$\boldsymbol{A}_{11}^1 = \begin{bmatrix} \mathcal{A}_{11} & \mathcal{A}_{12} \\ \mathcal{A}_{21} & \mathcal{A}_{22} \end{bmatrix}, \quad \boldsymbol{A}_{12}^1 = \begin{bmatrix} \mathcal{A}_{13} \\ \mathcal{A}_{23} \end{bmatrix}, \quad \boldsymbol{A}_{21}^1 = \begin{bmatrix} \mathcal{A}_{31} & \mathcal{A}_{32} \end{bmatrix}, \quad A_{22}^1 = \mathcal{A}_{33}^1. \tag{4.4}$$

Note that $\mathcal{A}_{33}$ has a superscript of 1. This is because $\mathcal{A}_{33}$ has contributions from both processors 1 and 2 while obtaining the linear system since it is shared. The other terms are local to processor 1. Also, $\boldsymbol{b}_1^1 = [\mathscr{b}_1 \quad \mathscr{b}_2]^T$ and $b_2^1 = \mathscr{b}_3^1$. Similarly, $\boldsymbol{A}^2$ and $\boldsymbol{b}^2$ are given by

$$\boldsymbol{A}^2 = \begin{bmatrix} \boldsymbol{A}_{11}^2 & \boldsymbol{A}_{12}^2 \\ \boldsymbol{A}_{21}^2 & \boldsymbol{A}_{22}^2 \end{bmatrix}, \quad \boldsymbol{b}^2 = \begin{bmatrix} \boldsymbol{b}_1^2 \\ \boldsymbol{b}_2^2 \end{bmatrix}, \tag{4.5}$$

where the blocks of $\boldsymbol{A}^2$ are given by

$$A_{11}^2 = \mathcal{A}_{33}^2, \quad \boldsymbol{A}_{12}^2 = \begin{bmatrix} \mathcal{A}_{34} & \mathcal{A}_{35} \end{bmatrix}, \quad \boldsymbol{A}_{21}^2 = \begin{bmatrix} \mathcal{A}_{43} \\ \mathcal{A}_{53} \end{bmatrix}, \quad \boldsymbol{A}_{22}^2 = \begin{bmatrix} \mathcal{A}_{44} & \mathcal{A}_{45} \\ \mathcal{A}_{54} & \mathcal{A}_{55} \end{bmatrix}, \tag{4.6}$$

and the components of the vector $\boldsymbol{b}^2$ are given by $b_1^2 = \mathscr{b}_3^2$ and $\boldsymbol{b}_2^2 = [\mathscr{b}_4 \quad \mathscr{b}_5]^T$. $\mathcal{A}$ and $\mathscr{b}$ in terms of their local components can be written as follows:

$$\mathcal{A} = \begin{bmatrix} \boldsymbol{A}_{11}^1 & \boldsymbol{A}_{12}^1 & 0 \\ \boldsymbol{A}_{21}^1 & A_{22}^1 + A_{11}^2 & \boldsymbol{A}_{12}^2 \\ 0 & \boldsymbol{A}_{21}^2 & \boldsymbol{A}_{22}^2 \end{bmatrix}, \quad \mathscr{b} = \begin{bmatrix} \boldsymbol{b}_1^1 \\ b_2^1 + b_1^2 \\ \boldsymbol{b}_2^2 \end{bmatrix}. \tag{4.7}$$

The most basic solution possible for this system, $\mathcal{A}\boldsymbol{x} = \mathscr{b}$ is $\boldsymbol{x} = c\mathscr{b}$, where the solution vector $\boldsymbol{x}$ is represented as c times $\mathscr{b}$, where $\mathscr{b}$ is a member of the Krylov subspace, and c is that value for which the norm of the residual is minimized or $\frac{\partial}{\partial c}\|\mathcal{A}\boldsymbol{x} - \mathscr{b}\| = 0$. The linear system is said to have one degree of freedom since we need to find out one unknown value, c. It is straightforward to show that $c = \langle \mathcal{A}\mathscr{b}, \mathscr{b} \rangle / \| \mathcal{A}\mathscr{b} \|^2$, where $\langle \bullet, \bullet \rangle$ represents the dot product operation and

$\| \bullet \|$ represents the norm. To find out c, the first step involves communicating the value corresponding to the shared node in the vector $\mathscr{l}$ so that both the processors have the correct value of $\mathscr{l}$ for that node. The local vectors after communication, $\boldsymbol{b}_c^1$ and $\boldsymbol{b}_c^2$ are given by

$$\boldsymbol{b}_c^1 = \begin{bmatrix} \boldsymbol{b}_1^1 \\ b_s \end{bmatrix}, \quad \boldsymbol{b}_c^2 = \begin{bmatrix} b_s \\ \boldsymbol{b}_2^2 \end{bmatrix}, \tag{4.8}$$

where $b_s = b_2^1 + b_1^2$ is the correct value corresponding to the shared node that would have been obtained directly during discretization had there been one processor. The next step would be to obtain the matrix-vector product locally in each processor. We denote the vectors obtained in this process as $\boldsymbol{w}^1$ and $\boldsymbol{w}^2$ in processors 1 and 2, respectively, where $\boldsymbol{w}^1 = \boldsymbol{A}^1 \boldsymbol{b}_c^1$ and $\boldsymbol{w}^2 = \boldsymbol{A}^2 \boldsymbol{b}_c^2$. Expanding this, we get

$$\boldsymbol{w}^1 = \begin{bmatrix} \boldsymbol{A}_{11}^1 & \boldsymbol{A}_{12}^1 \\ \boldsymbol{A}_{21}^1 & A_{22}^1 \end{bmatrix} \begin{bmatrix} \boldsymbol{b}_1^1 \\ b_s \end{bmatrix} = \begin{bmatrix} \boldsymbol{A}_{11}^1 \boldsymbol{b}_1^1 & + \boldsymbol{A}_{12}^1 b_s \\ \boldsymbol{A}_{21}^1 \boldsymbol{b}_1^1 & + A_{22}^1 b_s \end{bmatrix}, \tag{4.9}$$

and

$$\boldsymbol{w}^2 = \begin{bmatrix} A_{11}^2 & \boldsymbol{A}_{12}^2 \\ \boldsymbol{A}_{21}^2 & \boldsymbol{A}_{22}^2 \end{bmatrix} \begin{bmatrix} b_s \\ \boldsymbol{b}_2^2 \end{bmatrix} = \begin{bmatrix} A_{11}^2 b_s & + \boldsymbol{A}_{12}^2 \boldsymbol{b}_2^2 \\ \boldsymbol{A}_{21}^2 b_s & + \boldsymbol{A}_{22}^2 \boldsymbol{b}_2^2 \end{bmatrix}. \tag{4.10}$$

For simplicity, we represent these components as follows

$$\begin{aligned} &\boldsymbol{w}_{11,1}^1 = \boldsymbol{A}_{11}^1 \boldsymbol{b}_1^1, \qquad \boldsymbol{w}_{12,s}^1 = \boldsymbol{A}_{12}^1 b_s, \qquad w_{21,1}^1 = \boldsymbol{A}_{21}^1 \boldsymbol{b}_1^1, \qquad w_{22,s}^1 = A_{22}^1 b_s, \\ &w_{11,s}^2 = A_{11}^2 b_s, \qquad w_{12,2}^2 = \boldsymbol{A}_{12}^2 \boldsymbol{b}_2^2, \qquad \boldsymbol{w}_{21,s}^2 = \boldsymbol{A}_{21}^2 b_s, \qquad \boldsymbol{w}_{22,2}^2 = \boldsymbol{A}_{22}^2 \boldsymbol{b}_2^2. \end{aligned} \tag{4.11}$$

Therefore Eqs. (4.9) and (4.10) can be rewritten as

$$\boldsymbol{w}^1 = \begin{bmatrix} \boldsymbol{w}_{11,1}^1 & + \boldsymbol{w}_{12,s}^1 \\ w_{21,1}^1 & + w_{22,s}^1 \end{bmatrix} = \begin{bmatrix} \boldsymbol{w}_1^1 \\ w_2^1 \end{bmatrix}, \tag{4.12}$$

and

$$\boldsymbol{w}^2 = \begin{bmatrix} w_{11,s}^2 & + w_{12,2}^2 \\ \boldsymbol{w}_{21,s}^2 & + \boldsymbol{w}_{22,2}^2 \end{bmatrix} = \begin{bmatrix} w_1^2 \\ \boldsymbol{w}_2^2 \end{bmatrix}. \tag{4.13}$$

Since we have only one shared node in this example, w_2^1 and w_1^2 are scalars. These values are communicated to get the correct value corresponding to the shared node in $\boldsymbol{w}^1$ and $\boldsymbol{w}^2$, which are denoted by $\boldsymbol{w}_c^1$ and $\boldsymbol{w}_c^2$, and are given by

$$\boldsymbol{w}_c^1 = \begin{bmatrix} \boldsymbol{w}_1^1 \\ w_2^1 + w_1^2 \end{bmatrix}, \quad \boldsymbol{w}_c^2 = \begin{bmatrix} w_1^2 + w_2^1 \\ \boldsymbol{w}_2^2 \end{bmatrix}. \tag{4.14}$$

These ideas can be extended to dot products to find the value of c. We now increase the degree of freedom of the linear system to two by representing the solution vector $\boldsymbol{x}$ as follows:

$$\boldsymbol{x} = \begin{bmatrix} c^1 \boldsymbol{b}_1^1 \\ c^1 b_s \\ c^2 \boldsymbol{b}_2^2 \end{bmatrix}, \tag{4.15}$$

where c^1 and c^2 have to be optimized to get the best solution. Note that we still have used only one vector from the Krylov subspace. We show in our subsequent derivations that we can evaluate c^1 and c^2 using the vectors we obtained in Eqs (4.9) and (4.10) without performing extra matrix-vector products that have the largest contribution to the communication overhead. To find out the unknowns, first we need to evaluate the residual of the global linear system, which is given by

$$\mathscr{A}\boldsymbol{x} - \mathscr{b} = \begin{bmatrix} \boldsymbol{A}_{11}^1 & \boldsymbol{A}_{12}^1 & 0 \\ \boldsymbol{A}_{21}^1 & A_{22}^1 + A_{11}^2 & \boldsymbol{A}_{12}^2 \\ 0 & \boldsymbol{A}_{21}^2 & \boldsymbol{A}_{22}^2 \end{bmatrix} \begin{bmatrix} c^1 \boldsymbol{b}_1^1 \\ c^1 b_s \\ c^2 \boldsymbol{b}_2^2 \end{bmatrix} - \begin{bmatrix} \boldsymbol{b}_1^1 \\ b_s \\ \boldsymbol{b}_2^2 \end{bmatrix}. \tag{4.16}$$

We want to find out the values of c^1 and c^2 for which the norm of the residual is minimized or $\frac{\partial}{\partial c^1}\|\mathscr{A}\boldsymbol{x} - \mathscr{b}\| = 0$:

$$\begin{aligned} &\Big(\| \boldsymbol{A}_{11}^1 \boldsymbol{b}_1^1 + \boldsymbol{A}_{12}^1 b_s \|^2 + \| \boldsymbol{A}_{21}^1 \boldsymbol{b}_1^1 + A_{22}^1 b_s + A_{11}^2 b_s \|^2 + \| \boldsymbol{A}_{21}^2 b_s \|^2 \Big) c^1 \\ &\quad + \Big(\langle (\boldsymbol{A}_{21}^1 \boldsymbol{b}_1^1 + A_{22}^1 b_s + A_{11}^2 b_s), \boldsymbol{A}_{12}^2 \boldsymbol{b}_2^2 \rangle + \langle \boldsymbol{A}_{21}^2 b_s, \boldsymbol{A}_{22}^2 \boldsymbol{b}_2^2 \rangle \Big) c^2 = \\ &\langle (\boldsymbol{A}_{11}^1 \boldsymbol{b}_1^1 + \boldsymbol{A}_{12}^1 b_s), \boldsymbol{b}_1^1 \rangle + \langle (\boldsymbol{A}_{21}^1 \boldsymbol{b}_1^1 + A_{22}^1 b_s + A_{11}^2 b_s), b_s \rangle + \langle \boldsymbol{A}_{21}^2 b_s, \boldsymbol{b}_2^2 \rangle. \end{aligned} \tag{4.17}$$

Similarly, $\frac{\partial}{\partial c^2}\|\mathcal{A}\boldsymbol{x} - \mathscr{C}\| = 0$ yields

$$\begin{aligned}\Big(\langle\, (\boldsymbol{A}_{21}^1 \boldsymbol{b}_1^1 + A_{22}^1 b_s + A_{11}^2 b_s), \boldsymbol{A}_{12}^2 \boldsymbol{b}_2^2 \,\rangle + \langle\, \boldsymbol{A}_{22}^2 \boldsymbol{b}_2^2, \boldsymbol{A}_{21}^2 b_s \,\rangle \Big) c^1 + \\ \Big(\| \boldsymbol{A}_{12}^2 \boldsymbol{b}_2^2 \|^2 + \| \boldsymbol{A}_{22}^2 \boldsymbol{b}_2^2 \|^2 \Big) c^2 = \langle\, \boldsymbol{A}_{12}^2 \boldsymbol{b}_2^2, b_s \,\rangle + \langle\, \boldsymbol{A}_{22}^2 \boldsymbol{b}_2^2, \boldsymbol{b}_2^2 \,\rangle.\end{aligned} \tag{4.18}$$

Eq. (4.17) and Eq. (4.18) represent a linear system in c^1 and c^2 which can be easily evaluated. Using the notations defined in Eq. (4.11) we get

$$\begin{bmatrix} B_{11} & B_{12} \\ B_{21} & B_{22} \end{bmatrix} \begin{bmatrix} c^1 \\ c^2 \end{bmatrix} = \begin{bmatrix} k_1 \\ k_2 \end{bmatrix}, \tag{4.19}$$

where B_{11}, B_{12}, B_{21}, B_{22}, k_1 and k_2 are scalars whose values are as follows:

$$\begin{aligned} B_{11} &= \|\boldsymbol{w}_1^1\|^2 + (w_2^1 + w_{11,s}^2)^2 + \|\boldsymbol{w}_{21,s}^2\|^2, \\ B_{12} &= (w_2^1 + w_{11,s}^2) \times w_{12,2}^2 + \langle \boldsymbol{w}_{21,s}^2, \boldsymbol{w}_{22,2}^2 \rangle, \\ B_{21} &= (w_2^1 + w_{11,s}^2) \times w_{12,2}^2 + \langle \boldsymbol{w}_{21,s}^2, \boldsymbol{w}_{22,2}^2 \rangle, \\ B_{22} &= (w_{12,2}^2)^2 + \|\boldsymbol{w}_{22,2}^2\|^2, \\ k_1 &= \langle \boldsymbol{w}_1^1, \boldsymbol{b}_1^1 \rangle + (w_2^1 + w_{11,s}^2) \times b_s + \langle \boldsymbol{w}_{21,s}^2, \boldsymbol{b}_2^2 \rangle, \\ k_2 &= w_{12,2}^2 \times b_s + \langle \boldsymbol{w}_{22,2}^2, \boldsymbol{b}_2^2 \rangle. \end{aligned} \tag{4.20}$$

We do not need to perform any new matrix-vector product if the degree of freedom increases from 1 to 2. All the dot products in Eq. (4.20) involve vectors which are evaluated in the same processor. In other words, none of the dot products involve multiplying a vector evaluated by processor 1 with a vector evaluated by processor 2. Hence, only scalars need to be communicated across the shared node.

We go back to our 1D-heat conduction problem and assign values to f, q, and g such that $f = 4$, $q = 0.4$, and $g = 2$. The choice of values is arbitrary and is simply used to demonstrate that we get a noticeable improvement in the accuracy. We define the error as the norm of the residual normalized by

the norm of $\mathscr{b}$. For the one degree of freedom case, the error is 0.5107. When we increase the degrees of freedom to 2, the error comes out to be 0.4292. All we did more was communicate some scalars, multiply scalars and solve a 2×2 linear system that hardly adds to the communications and ended up getting up a more accurate result for one iteration.

To summarize the method, for a given linear system $\mathscr{A}\,\boldsymbol{x} = \mathscr{b}$, we represent the solution vector in terms of two unknowns c^1 and c^2 corresponding to each processor (there are two processors in our test case) instead of one unknown c. We show that this hardly adds to the communication overhead since we make use of the matrix-vector products which are already evaluated for the case with one constant but there is a noticeable improvement in accuracy. Although one needs to keep in mind that this is a very basic problem with one spatial dimension, two processors and one vector. The real challenge would be extending this method to more vectors in the Krylov subspace, or in other words increase the number of iterations. Other directions that can be explored are the extension to higher dimensions in space, and solve the system with more than two processors.

APPENDIX A

RBVMS FORMULATION

The RBVMS formulation used for comparison is provided in brief below, the details of which can be found in [37, 38, 54]. The weak formulation of the RBVMS is stated as follows. Find $u \in \mathcal{S}$ and $p \in \mathcal{P}$, such that for all $w \in \mathcal{W}$ and $q \in \mathcal{Q}$

$$B_G(w, q; u, p) + B_S(w, q; u, p) = F(w, q), \tag{A.1}$$

where

$$\begin{aligned}
B_G &= \int_\Omega \left[\rho w \cdot (\dot{u} + u \cdot \nabla u) + \nabla w : (-pI + \mu \nabla^s u) + q \nabla \cdot u\right] \mathrm{d}\Omega, \\
B_S &= \sum_{e \in I_e} \int_{\Omega^e} \left[\rho \nabla w : \left(\bar{\tau} u_\mathrm{p} \otimes (u_\mathrm{p} \cdot \nabla u) - u \otimes u_\mathrm{p} + \tau_\mathrm{C} \nabla \cdot u I\right) + \rho w \cdot \left(u_\mathrm{p} \cdot \nabla u\right) - u_\mathrm{p} \cdot \nabla q\right] \mathrm{d}\Omega, \\
F &= \int_{\Gamma_\mathrm{h}} w \cdot h \mathrm{d}\Gamma.
\end{aligned} \tag{A.2}$$

In this equation, B_G contains Galerkin's term whereas B_S are the stabilization added to allow for equal-order velocity and pressure functions and prevent convective instability associated with Galerkin's method. Other parameters appearing in (A.2) are defined as

$$\begin{aligned}
u_\mathrm{p} &= -\tau_\mathrm{M} \left(\dot{u} + u \cdot \nabla u + \frac{1}{\rho} \nabla p - \frac{\mu}{\rho} \nabla^2 u - f\right), \\
\tau_\mathrm{M} &= \left[\left(\frac{2 c_1}{\Delta t}\right)^2 + u \cdot \xi u + c_2 \left(\frac{\mu}{\rho}\right)^2 \xi : \xi\right]^{-\frac{1}{2}}, \\
\bar{\tau} &= \left(u_\mathrm{p} \cdot \xi u_\mathrm{p}\right)^{-\frac{1}{2}}, \\
\tau_\mathrm{C} &= \left[\mathrm{tr}\,(\xi)\, \tau_\mathrm{M}\right]^{-1}
\end{aligned} \tag{A.3}$$

in which $c_1 = 1$ and $c_2 = 3$, $\xi \in \mathbb{R}^{n_\mathrm{sd}} \times \mathbb{R}^{n_\mathrm{sd}}$ is covariant tensor obtained from a mapping between the physical and parent domains, and Δt is the time step size. The resulting equations are discretized using tetrahedral elements. To relate $\dot{u}$ to

u and integrate the resulting equations in time, the second order generalized-α method is adopted that has been explained in great detail earlier. We get a linear system similar to the MSS.

$$\begin{bmatrix} K & G \\ D & L \end{bmatrix} \begin{bmatrix} \Delta \dot{u} \\ \Delta p \end{bmatrix} = - \begin{bmatrix} R_M \\ R_C \end{bmatrix}, \tag{A.4}$$

where

$$\begin{aligned} K &= \frac{\partial R_M}{\partial \Delta \dot{u}}, \\ G &= \frac{\partial R_M}{\partial \Delta p}, \\ D &= \frac{\partial R_C}{\partial \Delta \dot{u}}, \\ L &= \frac{\partial R_C}{\partial \Delta p}. \end{aligned} \tag{A.5}$$

Unlike operator splitting techniques that time advance velocity first and then enforce divergence-free condition by solving a Poisson equation, the RBVMS solves for both at the same time during a single linear solve as implied by Eq. (A.4). Despite this difference, the sub-block matrix that relates pressure to continuity (L in Eq. (A.4) that arises from $u_{\mathrm{p}} \cdot \nabla q$ stabilization term in Eq. (A.2)) is identical to the discrete Laplacian operator that appears in the operator splitting technique. Note that this sub-block was zero in the linear system that arises from the SCVS formulation due to the lack of any stabilization term in our formulation (c.f., Eq. (3.11)). As a consequence of this zero sub-block, the tangent matrix is ill-conditioned, resulting in a lower rate of convergence for the SCVS in comparison to the RBVMS.

BIBLIOGRAPHY

[1] M. Esmaily and A. Mani, "Modal analysis of the behavior of inertial particles in turbulence subjected to stokes drag," *Modal analysis of the behavior of inertial particles in turbulence subjected to Stokes drag, Phys. Rev. Fluids*, vol. 5, p. 084303, Aug 2020.

[2] C. Meng, "A forked-accelerated simulation technique (FAST) for modeling blood flow in the cardiovascular system," Master's thesis, Cornell University, Ithaca, New York, 2020.

[3] J. N. Cuzzi, R. C. Hogan, J. M. Paque, and A. R. Dobrovolskis, "Size-selective concentration of chondrules and other small particles in protoplanetary nebula turbulence," *Size-selective concentration of chondrules and other small particles in protoplanetary nebula turbulence, The Astrophysical Journal*, vol. 546, no. 1, p. 496, 2001.

[4] M. N. Ardekani, G. Sardina, L. Brandt, L. Karp-Boss, R. Bearon, and E. Variano, "Sedimentation of inertia-less prolate spheroids in homogenous isotropic turbulence with application to non-motile phytoplankton," *Sedimentation of inertia-less prolate spheroids in homogenous isotropic turbulence with application to non-motile phytoplankton, Journal of Fluid Mechanics*, vol. 831, pp. 655–674, 2017.

[5] G. Falkovich, A. Fouxon, and M. Stepanov, "Acceleration of rain initiation by cloud turbulence," *Acceleration of rain initiation by cloud turbulence, Nature*, vol. 419, no. 6903, pp. 151–154, 2002.

[6] M. Pinsky, A. Khain, and M. Shapiro, "Stochastic effects of cloud droplet hydrodynamic interaction in a turbulent flow," *Stochastic effects of cloud droplet hydrodynamic interaction in a turbulent flow, Atmospheric research*, vol. 53, no. 1-3, pp. 131–169, 2000.

[7] R. A. Shaw, W. C. Reade, L. R. Collins, and J. Verlinde, "Preferential concentration of cloud droplets by turbulence: Effects on the early evolution of cumulus cloud droplet spectra," *Preferential concentration of cloud droplets by turbulence: Effects on the early evolution of cumulus cloud droplet spectra, Journal of the atmospheric sciences*, vol. 55, no. 11, pp. 1965–1976, 1998.

[8] K. Guseva, A. Daitche, U. Feudel, and T. Tél, "History effects in the sedimentation of light aerosols in turbulence: The case of marine snow," *History effects in the sedimentation of light aerosols in turbulence: The case of marine snow, Physical Review Fluids*, vol. 1, no. 7, p. 074203, 2016.

[9] S. Balachandar and J. K. Eaton, "Turbulent dispersed multiphase flow," *Turbulent dispersed multiphase flow, Annual review of fluid mechanics*, vol. 42, pp. 111 – 133, 2010.

[10] J. K. Eaton and J. Fessler, "Preferential concentration of particles by turbulence," *Preferential concentration of particles by turbulence, International Journal of Multiphase Flow*, vol. 20, pp. 169–209, 1994.

[11] H. Pouransari and A. Mani, "Effects of preferential concentration on heat transfer in particle-based solar receivers," *Effects of preferential concentration on heat transfer in particle-based solar receivers*, vol. 139, no. 2, 2017.

[12] E. Farbar, I. D. Boyd, and M. Esmaily-Moghadam, "Monte carlo modeling of radiative heat transfer in particle-laden flow," *Monte Carlo modeling of radiative heat transfer in particle-laden flow, Journal of Quantitative Spectroscopy and Radiative Transfer*, vol. 184, pp. 146–160, 2016.

[13] J. Bec, "Fractal clustering of inertial particles in random flows," *Fractal clustering of inertial particles in random flows,Physics of fluids*, vol. 15, no. 11, pp. L81–L84, 2003.

[14] W. C. Reade and L. R. Collins, "Effect of preferential concentration on turbulent collision rates," *Physics of Fluids*, vol. 12, no. 10, pp. 2530–2540, 2000.

[15] E. Calzavarini, M. Cencini, D. Lohse, F. Toschi, *et al.*, "Quantifying turbulence-induced segregation of inertial particles," *Quantifying turbulence-induced segregation of inertial particles, Physical review letters*, vol. 101, no. 8, p. 084504, 2008.

[16] S. Mendis, P. Puska, B. Norrving, W. H. Organization, *et al.*, *Global atlas on cardiovascular disease prevention and control*. World Health Organization, 2011.

[17] A. Blalock and H. B. Taussig, "The surgical treatment of malformations of the heart: in which there is pulmonary stenosis or pulmonary atresia," *Journal of the American Medical Association*, vol. 128, no. 3, pp. 189–202, 1945.

[18] M. Esmaily Moghadam, F. Migliavacca, I. E. Vignon-Clementel, T.-Y. Hsia, A. L. Marsden, M. of Congenital Hearts Alliance (MOCHA) Investigators, *et al.*, "Optimization of shunt placement for the norwood surgery using multi-domain modeling," *Journal of biomechanical engineering*, vol. 134, no. 5, 2012.

[19] K. Pekkan, B. Whited, K. Kanter, S. Sharma, D. De Zelicourt, K. Sundareswaran, D. Frakes, J. Rossignac, and A. P. Yoganathan, "Patient-specific surgical planning and hemodynamic computational fluid dynamics optimization through free-form haptic anatomy editing tool (surgem)," *Medical & biological engineering & computing*, vol. 46, no. 11, pp. 1139–1152, 2008.

[20] A. J. Petersen, L. Baker, and F. Coletti, "Experimental study of inertial particles clustering and settling in homogeneous turbulence," *Experimental study of inertial particles clustering and settling in homogeneous turbulence, Journal of Fluid Mechanics*, vol. 864, pp. 925–970, 2019.

[21] E. W. Saw, R. A. Shaw, S. Ayyalasomayajula, P. Y. Chuang, and A. Gylfason, "Inertial clustering of particles in high-reynolds-number turbulence," *Inertial clustering of particles in high-Reynolds-number turbulence, Physical review letters*, vol. 100, no. 21, p. 214501, 2008.

[22] Experimental, J. P. numerical investigation of inertial particle clustering in isotropic turbulence, Salazar, J. De Jong, L. Cao, S. H. Woodward, H. Meng, and L. R. Collins, "Experimental and numerical investigation of inertial particle clustering in isotropic turbulence," *Journal of Fluid Mechanics*, vol. 600, p. 245, 2008.

[23] A. Aliseda, A. Cartellier, F. Hainaux, and J. C. Lasheras, "Effect of preferential concentration on the settling velocity of heavy particles in homogeneous isotropic turbulence," *Effect of preferential concentration on the settling velocity of heavy particles in homogeneous isotropic turbulence, Journal of Fluid Mechanics*, vol. 468, pp. 77–105, 2002.

[24] J. R. Fessler, J. D. Kulick, and J. K. Eaton, "Preferential concentration of heavy particles in a turbulent channel flow," *Preferential concentration of heavy particles in a turbulent channel flow, Physics of Fluids*, vol. 6, no. 11, pp. 3742–3749, 1994.

[25] S. Sundaram and L. R. Collins, "Collision statistics in an isotropic particle-laden turbulent suspension. part 1. direct numerical simulations," *Collision statistics in an isotropic particle-laden turbulent suspension. Part 1. Direct numerical simulations, Journal of Fluid Mechanics*, vol. 335, pp. 75–109, 1997.

[26] S. Goto and J. Vassilicos, "Sweep-stick mechanism of heavy particle clustering in fluid turbulence," *Sweep-stick mechanism of heavy particle clustering in fluid turbulence, Physical review letters*, vol. 100, no. 5, p. 054503, 2008.

[27] Y. Tagawa, J. M. Mercado, V. N. Prakash, E. Calzavarini, C. Sun, and D. Lohse, "Three-dimensional lagrangian voronoï analysis for clustering of particles and bubbles in turbulence," *Three-dimensional Lagrangian Voronoï analysis for clustering of particles and bubbles in turbulence, Journal of fluid mechanics*, vol. 693, pp. 201–215, 2012.

[28] B. Ray and L. R. Collins, "Preferential concentration and relative velocity statistics of inertial particles in navier-stokes turbulence with and without filtering," *Preferential concentration and relative velocity statistics of inertial particles in Navier-Stokes turbulence with and without filtering, Journal of fluid mechanics*, vol. 680, p. 488, 2011.

[29] K. D. Squires and J. K. Eaton, "Preferential concentration of particles by turbulence," *Preferential concentration of particles by turbulence, Physics of Fluids A: Fluid Dynamics*, vol. 3, no. 5, pp. 1169–1178, 1991.

[30] E. Balkovsky, G. Falkovich, and A. Fouxon, "Intermittent distribution of inertial particles in turbulent flows," *Intermittent distribution of inertial particles in turbulent flows, Physical Review Letters*, vol. 86, no. 13, p. 2790, 2001.

[31] J. Bec, K. Gawdzki, and P. Horvai, "Multifractal clustering in compressible flows," *Multifractal clustering in compressible flows, Physical review letters*, vol. 92, no. 22, p. 224501, 2004.

[32] A. Robinson, "On the motion of small particles in a potential field of flow," *On the motion of small particles in a potential field of flow, Communications on Pure and Applied Mathematics*, vol. 9, no. 1, pp. 69–84, 1956.

[33] M. R. Maxey, "The gravitational settling of aerosol particles in homogeneous turbulence and random flow fields," *The gravitational settling of aerosol particles in homogeneous turbulence and random flow fields, Journal of fluid mechanics*, vol. 174, pp. 441–465, 1987.

[34] J. C. Hunt, A. A. Wray, and P. Moin, "Eddies, streams, and convergence zones in turbulent flows," *Eddies, streams, and convergence zones in turbulent flows, Proceedings of the Summer Program*, pp. 193–208, 1988.

[35] Y. Dubief and F. Delcayre, "On coherent-vortex identification in turbulence," *On coherent-vortex identification in turbulence, Journal of turbulence*, vol. 1, no. 1, pp. 011–011, 2000.

[36] D. A. Steinman, Y. Hoi, P. Fahy, L. Morris, M. T. Walsh, N. Aristokleous,

A. S. Anayiotos, Y. Papaharilaou, A. Arzani, S. C. Shadden, *et al.*, "Variability of computational fluid dynamics solutions for pressure and flow in a giant aneurysm: the asme 2012 summer bioengineering conference cfd challenge," *Journal of biomechanical engineering*, vol. 135, no. 2, 2013.

[37] A. N. Brooks and T. J. Hughes, "Streamline upwind/Petrov-Galerkin formulations for convection dominated flows with particular emphasis on the incompressible Navier-Stokes equations," *Computer methods in applied mechanics and engineering*, vol. 32, no. 1-3, pp. 199–259, 1982.

[38] Y. Bazilevs, V. Calo, J. Cottrell, T. Hughes, A. Reali, and G. Scovazzi, "Variational multiscale residual-based turbulence modeling for large eddy simulation of incompressible flows," *Computer methods in applied mechanics and engineering*, vol. 197, no. 1-4, pp. 173–201, 2007.

[39] M.-C. Hsu, Y. Bazilevs, V. M. Calo, T. E. Tezduyar, and T. J. Hughes, "Improving stability of stabilized and multiscale formulations in flow simulations at small time steps," *Computer Methods in Applied Mechanics and Engineering*, vol. 199, no. 13-16, pp. 828–840, 2010.

[40] M. Rosenfeld, "Utilization of Fourier decomposition for analyzing time-periodic flows," *Computers & fluids*, vol. 24, no. 4, pp. 349–368, 1995.

[41] M. R. Maxey and J. J. Riley, "Equation of motion for a small rigid sphere in a nonuniform flow," *Equation of motion for a small rigid sphere in a nonuniform flow, The Physics of Fluids*, vol. 26, no. 4, pp. 883–889, 1983.

[42] G. P. Langlois, M. Farazmand, and G. Haller, "Asymptotic dynamics of inertial particles with memory," *Journal of nonlinear science*, vol. 25, no. 6, pp. 1225–1255, 2015.

[43] C. Coimbra and R. Rangel, "General solution of the particle momentum equation in unsteady *s*tokes flows," *Journal of Fluid Mechanics*, vol. 370, pp. 53–72, 1998.

[44] M. Van Hinsberg, J. ten Thije Boonkkamp, and H. J. Clercx, "An efficient, second order method for the approximation of the basset history force," *Journal of Computational Physics*, vol. 230, no. 4, pp. 1465–1478, 2011.

[45] T. J. Hughes, W. K. Liu, and A. Brooks, "Finite element analysis of incompressible viscous flows by the penalty function formulation," *Journal of computational physics*, vol. 30, no. 1, pp. 1–60, 1979.

[46] F. Brezzi and K.-J. Bathe, "A discourse on the stability conditions for mixed finite element formulations," *Computer methods in applied mechanics and engineering*, vol. 82, no. 1-3, pp. 27–57, 1990.

[47] T. E. Tezduyar, "Stabilized finite element formulations for incompressible flow computations," in *Advances in applied mechanics*, vol. 28, pp. 1–44, Elsevier, 1991.

[48] O. A. Ladyzhenskaya, *The mathematical theory of viscous incompressible flow*, vol. 2. Gordon and Breach New York, 1969.

[49] I. Babuška, "Error-bounds for finite element method," *Numerische Mathematik*, vol. 16, no. 4, pp. 322–333, 1971.

[50] F. Brezzi, "On the existence, uniqueness and approximation of saddle-point problems arising from Lagrangian multipliers," *Publications mathématiques et informatique de Rennes*, no. S4, pp. 1–26, 1974.

[51] Y. Saad and M. H. Schultz, "GMRES: A generalized minimal residual algorithm for solving nonsymmetric linear systems," *SIAM Journal on scientific and statistical computing*, vol. 7, no. 3, pp. 856–869, 1986.

[52] H. Si, "Tetgen, a Delaunay-based quality tetrahedral mesh generator," *ACM Transactions on Mathematical Software (TOMS)*, vol. 41, no. 2, pp. 1–36, 2015.

[53] A. Updegrove, N. M. Wilson, J. Merkow, H. Lan, A. L. Marsden, and S. C. Shadden, "Simvascular: an open source pipeline for cardiovascular simulation," *Annals of biomedical engineering*, vol. 45, no. 3, pp. 525–541, 2017.

[54] M. Esmaily-Moghadam, Y. Bazilevs, and A. L. Marsden, "A bi-partitioned iterative algorithm for solving linear systems arising from incompressible flow problems," *Computer Methods in Applied Mechanics and Engineering*, vol. 286, pp. 40–62, 2015.

[55] M. Esmaily-Moghadam, Y. Bazilevs, and A. L. Marsden, "A new preconditioning technique for implicitly coupled multidomain simulations with applications to hemodynamics," *Computational Mechanics*, vol. 52, no. 5, pp. 1141–1152, 2013.

[56] M. Esmaily-Moghadam, Y. Bazilevs, and A. Marsden, "Impact of data distribution on the parallel performance of iterative linear solvers with em-

phasis on CFD of incompressible flows," *Computational Mechanics*, vol. 55, no. 1, pp. 93–103, 2015.

[57] J. R. Womersley, "Method for the calculation of velocity, rate of flow and viscous drag in arteries when the pressure gradient is known," *The Journal of physiology*, vol. 127, no. 3, p. 553, 1955.

[58] K. E. Jansen, C. H. Whiting, and G. M. Hulbert, "A generalized-α method for integrating the filtered Navier–Stokes equations with a stabilized finite element method," *Computer methods in applied mechanics and engineering*, vol. 190, no. 3-4, pp. 305–319, 2000.